Controlled synthesis of superparamagnetic iron oxide nanoparticles in the presence of poly(acrylic acid)

by

Miray Demirer

A Thesis Submitted to the
Graduate School of Engineering
in Partial Fulfillment of the Requirements for
the Degree of

Master of Science
in
Material Science&Engineering

Koc University

September 2006

Koc University

Graduate School of Sciences and Engineering

This is to certify that I have examined this copy of a master's thesis by

Miray Demirer

and have found that it is complete and satisfactory in all respects,
and that any and all revisions required by the final
examining committee have been made.

Committee Members:

_____

Havva Yagci Acar, Ph. D. (Advisor)

_____

A. Levent Demirel, Ph. D.

_____

Mehmet S. Somer, Ph. D.

Date: _____

ABSTRACT

Superparamagnetic iron oxide nanoparticles (SPIO) have been widely studied for a variety of biomedical applications such as magnetic resonance imaging (MRI), drug and gene delivery, hyperthermia and magnetic separation. Each application requires a specific size and surface chemistry in addition to stability. Therefore, controlling particle size and size distribution, providing functional surfaces and preventing particle aggregation are the key issues in this field.

Coating magnetic cores with polymeric materials to control particle size is one of the commonly used methods in recent years. In this project, poly (acrylic acid) sodium salt is used as a polymeric stabilizer. Poly (acrylic acid)-stabilized superparamagnetic iron oxide nanoparticles were synthesized by treating iron salts with ammonium hydroxide in water in the presence of PAA. Major goal of this research is to control particle size and stability through the control of reaction variables. Primarily, the influence of reaction variables, namely, iron concentration, reactive (COOH)/iron mole ratio, base (NH_4OH) amount and polymer molecular weight, on hydrodynamic size, stability and magnetic nature of the particles was investigated. In order to design best set of experiments and correlate the results to variables, statistical programs Design Expert 7.0 and Minitab14 were used. Through the use of deducted mathematical equation relating effective factors to the size, we achieved stable aqueous SPIOs with controlled size both in the small and ultrasmall size regime. In addition, the choice of PAA as the coating material provided functional groups on the surface for attachment of desired molecules and pH responsive nature to the SPIOs.

Stability and small sizes of the SPIOs provide a potential for the achievement of molecular targeting and contrast enhancement for MRI. Another goal of this project is to test the suitability of these particles for in vivo applications such as targeted and non-

targeted imaging and therapy. For this purpose, in vitro cell-studies and MRI imaging were carried out with the prepared PAA-coated iron oxide nanoparticles with different hydrodynamic sizes (30, 70, 110nm). HeLa and MCF-7 cancer cells were incubated with our samples and cell viabilities were measured by MTT assay. Preliminary results indicate non-toxic behavior of the particles to the cells. MRI investigation indicated potential for contrast enhancement.

ÖZET

Süperparamanyetik demir oksit nanoparçacıkları manyetik rezonans görüntüleme, manyetik ayrıştırma, vücuda ilaç ve gen göndermeye kadar pek çok biyomedikal sahada kullanılmaktadır. Her biyomedikal uygulama için belli parçacık büyüklüğü, yüzey kimyası gerekmekte ve hemen her uygulama için parçacıkların kararlılığı önemli olmaktadır. Bu yüzden, parçacık boyu ve dağılımının kontrol edilmesi, uygun özelliklerde parçacık yüzeyi elde edilmesi ve parçacıkların topaklaşması sonucu parçacık boyunun büyümesinin engellenmesi bu sahada en çok çalışılan konulardır.

Son yıllarda parçacık boyunu kontrol edebilmek için uygulanan yöntemlerden birisi, manyetik çekirdekleri polimerik malzemelerle kaplayarak kararlılığının sağlanmasıdır. Bu araştırmada poli(akrilik asit) sodyum tuzu polimeri bu amaç için kullanılmıştır. Demir tuzlarının su ve pol(iakrilik asit) sodyum tuzu bulunan ortamda amonyum hidroksit ile muamele edilerek oksitlenmesi sağlanmış ve pol(iakrilik asit) ile stabilize edilmiş demir oksit nanoparçacıkları sentezlenmiştir. Bu araştırmanın asıl amacı, parçacık boyu ve kararlılığını reaksiyonda kullanılan kimyasallarin konsantrasyonlarını değiştirerek kontrol etmektir. Toplam demir konsantrasyonu, reaktif (COOH)/demir mol oranı, baz miktarı (NH_4OH) ve polimerin moleküler ağırlığı olmak üzere dört faktör kontrol edilmiş ve bu faktörlerin parçacık boyuna (hidrodinamik), kararlılığına ve manyetizasyonuna olan etkisi incelenmiştir. İstatistiksel olarak bu faktörlerin etkilerini gözlemleyebilmek için Design Expert 7.0 ve Minitab 14 Release programları kullanılmıştır. Bu veriler kullanılarak parçacık boyu ve parçacık boyuna etki eden önemli faktörler arasında matematiksel bir ifade elde edilmiştir. Daha sonra yapılan denemelerde bu matematiksel ifadenin parçacık boyunu tahmin edebilmekte yeterli olduğu ve kararlı, suda çözünen süperparamanyetik demir oksit nanoparçacıklarının boyutunun kontrol edilebildiği görülmüştür. Ayrıca, poliakrilik asit sodyum tuzu seçilerek parçacıklarda pH'a duyarlı bir yüzey yaratılmış ve

yüzeydeki karboksilik asit gruplari aracılığıyla başka moleküllerin de kimyasal olarak bağlanabilmesi sağlanmıştır.

Sentezlenen küçük ve kararlı süperparamanyetik demir oksit nanoparçacıkları belli organlara ilaç gönderme ve manyetik rezonans görüntülemede kontrast yaratma potansiyeline sahiptir. Bunun için 30,70 ve 110 nanometrede elde edilen poli(akrilik asit) kaplı parçacıklarıyla in vitro hücre çalışmaları ve manyetik rezonans görüntüleme yapılmıştır. Parçacıklar, HeLa ve MCF-7 kanser hücreleri ile inkübe edilerek, MTT analizi ile hücre canlılıklarına bakılmıştır. İlk çalışmalar, sentezlenen parçacıkların toksik olmadığını göstermektedir. Ayrıca, parçacıkların manyetik rezonans görüntüleme için de uygun oldukları görülmüştür.

ACKNOWLEDGEMENTS

I would like to thank my advisor Assist. Prof. Havva Funda Yagci Acar for all her support and motivation during my research. It was a great chance for me to start an academic career under supervision of such a positive person. I would also like to thank Assist. Prof. A.Levent Demirel and Prof. Mehmet Somer for not only being my committee members, but also for their helpful and friendly approach to my problems.

I also have to thank my lab mates Berkut Ay Gunel, Onur Kaleli for their friendship and help during experimental part; Ozlem Tekmek for her cute curiosity and friendship; Feyza Selcuk for her encouragement and friendship; Serdar Celebi for his support in ICP analysis and friendly attitude. I would thank Ilkin Kokal and Selcuk Acar (X-Ray Man) for teaching me how to use XRD. Also, I have to thank Muharrem Guler for his help about all lab equipment.

For instrumental analysis, I would like to thank to Orhan Kamer from Istanbul Technical University for VSM studies, Emel Yilgor for TGA analysis, Sule Ozdas and Assis. Prof. Halil Kavakli for their support in cell studies, Cleva Ow-Yang and Mehmet Ali Gulgun for SEM, Cengiz Baycu for TEM and American Hospital for MRI studies.

Additionaly, I want to thank Bora Akcay for his endless care, understanding and support in all cases for two years. Also, I would like to thank Irem Kocaer for welcoming me her home anytime.

Finally, I want to thank my parents Deniz and Umit Demirer, and my sister Petek Demirer; to my grandparents Ferhan and Atilla Akcadogan for their everlasting love and patience. Without mum, this thesis would not be possible.

TABLE OF CONTENTS

LIST OF TABLES

LIST OF FIGURES

Chapter 1

INTRODUCTION

Nanoparticles having smaller size and larger surface area exhibit different physical and chemical properties from those of relatively larger nanoparticles. In the last decade, magnetic nanoparticles attracted tremendous attention due to unique size dependent properties and created new avenues for numerous applications from loud speakers to medicine. Superparamagnetic iron oxide nanoparticles (SPIONs) with combined properties of high magnetic saturation and biocompatibility generated a great excitement in the medicine and biotechnology area [1,2]. Magnetic nature of SPIOs means two important modes of application: Detection and separation in these fields. They are currently being used for magnetic resonance imaging (MRI) and magnetic separation, and showing very promising results for magnetic drug delivery, magnetic transfection and hyperthermia (thermal cancer therapy) [3,4].

Each application requires a different set of properties in terms of particle size and surface chemistry. In addition, size distribution and particle aggregation is an important issue to be dealt with. Yet, controlling these properties is not trivial and many times what the existing systems offer is the limitation in front of the new applications or their success [5,6,7].

1.1 Magnetism

"Magnetism" is basically about the response of a material in an external magnetic field. Net magnetization of the material occurs when the electron spins in the material align in the direction of the applied field, and is formulized as follows

$$B = H + 4\pi M$$

where H is the applied magnetic field intensity and B is the response from the material called magnetic flux density. Magnetization (M) is the magnetic moment per unit volume that depends on the magnetic moments of the constituent atoms, as well as their interaction with each other. M can be related to H through

$$M = \chi \cdot H$$

where χ is magnetic susceptibility and indicate how well the material response to the applied field.

The differences in electron configuration of elements determine the nature and magnitude of the atomic magnetic moments, and the differing magnetic properties of various materials. Several forms of magnetic behavior have been observed in different materials such as paramagnetism, ferromagnetism, antiferromagnetism and ferrimagnetism.

Paramagnetic materials are attracted when subjected to an applied magnetic field. Paramagnetism requires individual atoms to have permanent dipole moments, which typically implies an unpaired electron in the atomic or molecular orbitals. In pure paramagnetism, these atomic dipoles do not interact with one another and are randomly oriented in the absence of an external field, resulting in zero net moment (Figure 1.1a).

Yet, in an applied magnetic field these dipoles align in the direction of the field causing a net magnetization of the material (Figure 1.1b).

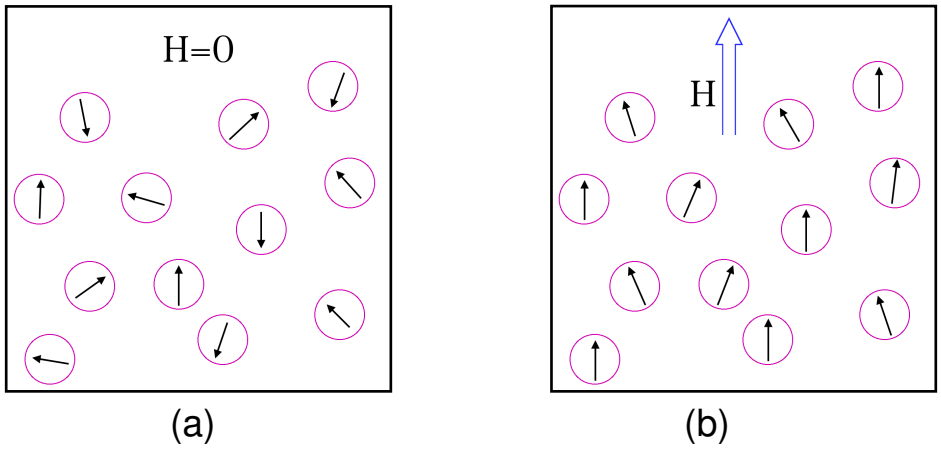

Figure 1.1: Orientation of atomic dipoles a) in the absence and b) in the presence of external magnetic field.

Paramagnetic behavior can also be observed in ferromagnetic materials that are above their Curie temperature. This critical temperature refers to a characteristic property of a ferromagnetic material above which material loses its ability to possess net magnetization in the absence of an external magnetic field. As the temperature increase from below the Curie point, increasing thermal fluctuations destroy the alignment of dipoles, until the net magnetization becomes zero at and above the Curie point. Above the Curie point, the material is purely paramagnetic.

Ferromagnetic materials typically show a hysteresis loop in magnetization curve. After the removal of external magnetic field, material retains some magnetization creating a hysteresis loop. This is called remanent magnetization (M_{rs}). The strength of the field in the opposite direction is called coercivity, H_c, which is applied until there is no magnetization

remaining. The relationship between magnetic field strength (H) and magnetic flux density (B) is not linear in such materials. If the relationship between the two is plotted for increasing levels of field strength, it will follow a curve up to a point where further increases in magnetic field strength will result in no further change in flux density. This condition is called saturation magnetization (M_s). A full hysteresis loop is formed by applying and removing the field to saturation in the negative direction, then applying it again in the positive direction (Figure 1.2).

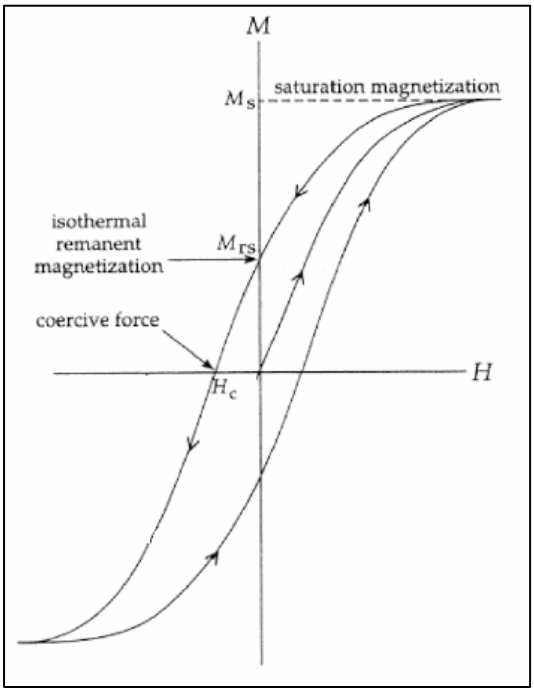

Figure 1.2: A schematic diagram of a hysteresis loop.

Superparamagnetism is a phenomenon by which magnetic materials may exhibit a behavior similar to paramagnetism even below Curie temperature. Generally, these are

single domain, single crystal nanoparticles of 10nm or less (Figure 1.3). In paramagnetic materials where spin alignment happens in domains, in superparamagnetic materials, the magnetic moment of the entire crystallite tends to align with the magnetic field creating a higher saturation value. Iron oxide nanoparticles, magnetite (Fe_3O_4) and maghemite (γ–Fe_2O_3), show superparamagnetic behavior at room temperature, and are biocompatible and biodegradable so are widely studied in biomedical field (Table 1.1).

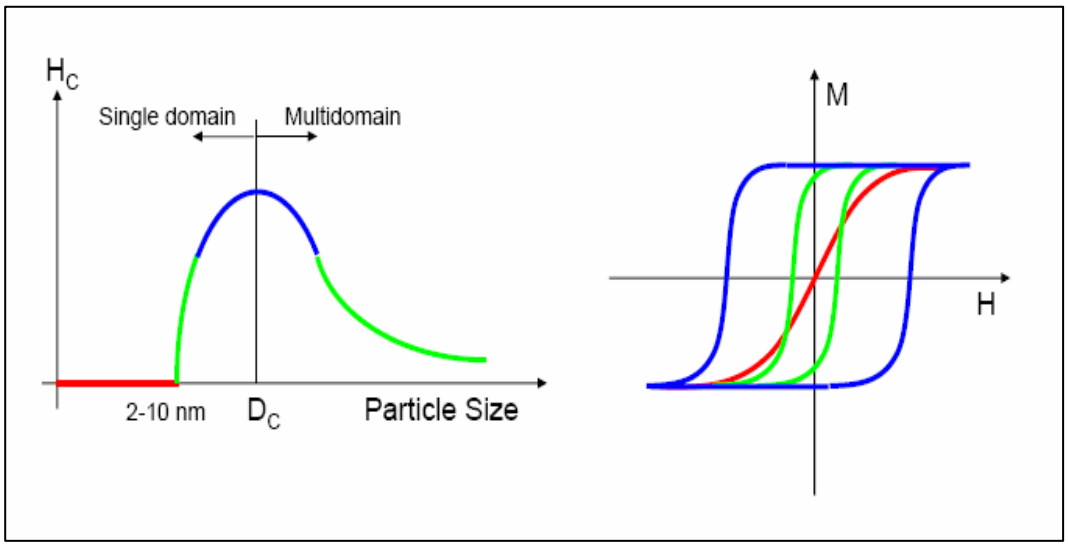

Figure 1.3: Magnetic properties of nanostructured materials: Ferromagnetism (blue), paramagnetism (green), Superparamagnetism (red).

Oxide	Color	Tc (K)	Msat at 300 K (J/T.kg)
Magnetite (Fe_3O_4)	black	850	92-100
Maghemite (γ-Fe_2O_3)	dark brown	820-986	60-80

Table 1.1. Properties of iron oxides [8].

1.2 Applications

SPIOs (usually γ-Fe_2O_3 and Fe_3O_4) possess high magnetic saturation with no remanence and coercivity. They are addressable by magnetic field meaning can be dragged by a magnet causing magnetic separation or localization, and/or can be magnetically detected.

SPIOs are core-shell structures where magnetic iron oxide cores are coated with a shell. Simply, magnetic core is responsible from the magnetic properties and the shell responsible from the stabilization of these magnetic cores and suspension of the particles in a carrier liquid. Depending on the application the carrier liquid changes so as the shell chemistry. For many in vivo applications aqueous suspensions are required. Therefore, dextran, starch and poly (vinyl alcohol) (PVA) like biocompatible and water soluble coatings are utilized as the coating [9,10,11]. For other applications, poly (styrene) (PS) or silica like coatings are also utilized [12,13].

Another important property for application is the particle size which is generally the hydrodynamic size. Nanoparticles are generally not in the form of single core-shell

structures but in aggregated forms. Size of these aggregates in the hydrated form is the generally mentioned *size* for these SPIOs (Figure 1.4).

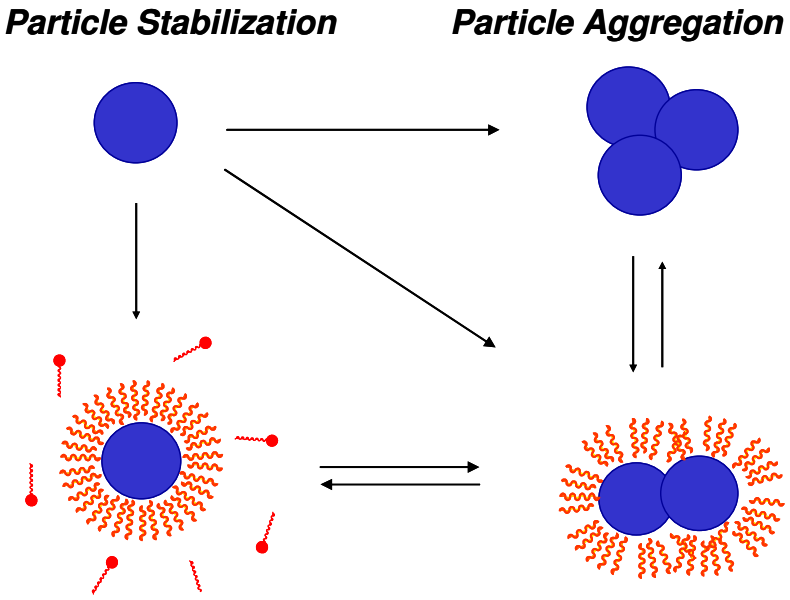

Figure 1.4: Core-shell structure.

The concept of exploitation of biocompatible magnetic nanoparticles (in the form of ferrofluids) with diagnosis and therapeutic purposes is being considered by a growing number of researchers in biomedical areas. In vivo, particles larger than 100 nanometers are taken up by the reticuloendothelial system (RES), a network of cells lining blood vessels whose function is to remove foreign substances from the bloodstream. These particles are directly taken to liver and spleen that constitute the RES system preventing the accumulation in other targeting organs [14]. Thus, ability to control particle size is a key

issue that would enable the use of nanoparticles for target specific applications as well as broader in vivo use.

SPIOs are routinely applied as negative contrast agents in magnetic resonance imaging (MRI). These particles shorten the proton relaxation times (T1 and T2) of the tissues that they occupy. If they shorten the T2 more than T1 they produce a dark image at the local site (Figure 1.5) and the agent is called *negative* contrast agent. If they produce a bright image, they are called as *positive* contrast agent (Figure 1.6). In the body, nanoparticles are internalized by macrophages of the reticuloendothelial system (RES), the part of the immune system, and taken to the liver. Therefore SPIOs are good contrast agents for the liver. Intake of the SPIOs from blood by phagocytic macrophages depends on many factors one of which is particle size. As the size of the particles reduce, they escape from macrophages, their blood circulation time increase and the probability of uptake by other organs increase. SPIOs with different sizes and coating materials are developed for the imaging of different tissues. Some of these are commercially available and some are in still clinical trial phase (Table 1.2) [15,16].

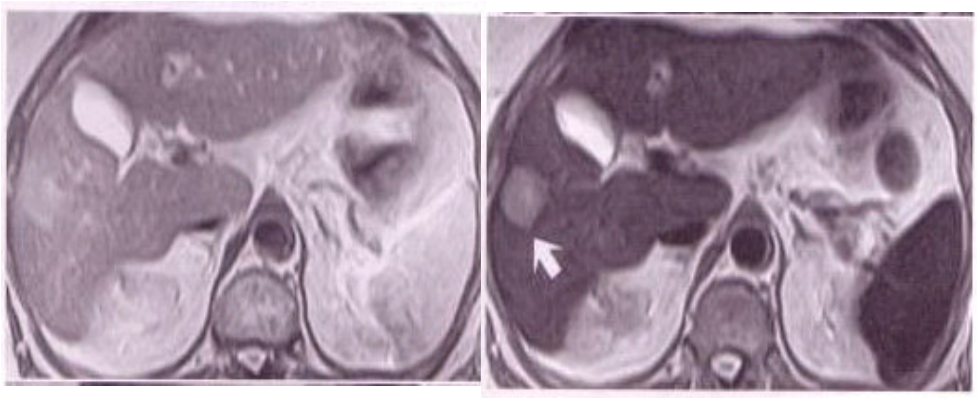

Figure 1.5: Contrast enhancement:
(Left) Before SPIO injection, (Right) After SPIO injection [17].

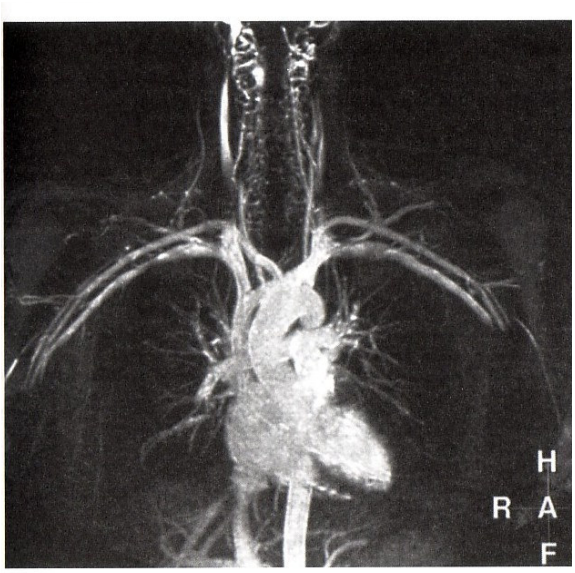

Figure 1.6: MRA of the thoracic region following administration of USPIO [18].

Agent	Shell	Size (nm)	Contrast	Application	Company	Status
Supravist/SHU555C	Carboxydextran	20	Positive	MR angiography	Schering	Phase II
Combidex/Sinerem	Dextran	25	Positive	Lymphoma, Plaque,MS	AMI/Guerbet	Phase II/III
Clariscan	Dextran-PEG	25	Positive	Coronary angiography	Amersham	Phase III
Feridex	Dextran	150	Negative	Liver imaging	AMI	Marketed
Lumirem/Gastromark	Silica	300	Negative	GI bowel imaging	Guerbet	Marketed
Abdoscan	Sulfonated PS-crosslinked	3000	Negative	GI bowel imaging	Nycomed/Amersham	Marketed

Table 1.2: SPIO contrast agents.

SPIOs when in large sizes (few hundred nm to microns) can be easily dragged by an external magnet therefore found applications for magnetic separation of cells, DNA/RNA, proteins, pathogens etc. (Dynal®, Chemicell®, MACS®). These commercial particles are generally coated with PS, silica, fatty acid, starch, dextran; etc where also terminal functional groups are utilized for covalent immobilization of ligands that could bind a specific biomolecule that would be separated [19]. Similar approach is also being investigated in therapy, where drugs were loaded on SPIOs through electrostatic or covalent binding and are guided to a specific site in the body with an external magnet (Figure 1.7). Magnetic delivery of anticancer drugs is especially an interest since it is a promising method that could prevent the harmful effects of chemotherapy on normal cells.

SPIOs are also being investigated for hyperthermia which is a thermal method for cancer treatment. In this approach, magnetic particles are localized in the tumor with an external magnet and are heated by applying an AC magnetic field of sufficient strength and frequency. Heat generated within the tumor destroys it. Clinical trials of Andreas et al are showing very promising results [20]. These particles are generally around 200 nm-1micron range. Smaller particles, less than 200nm are being investigated for drug delivery utilizing the phagocytic pathway without an external magnet. Delivery of oligonucleotides and chemotherapy are experimental extensions in this field.

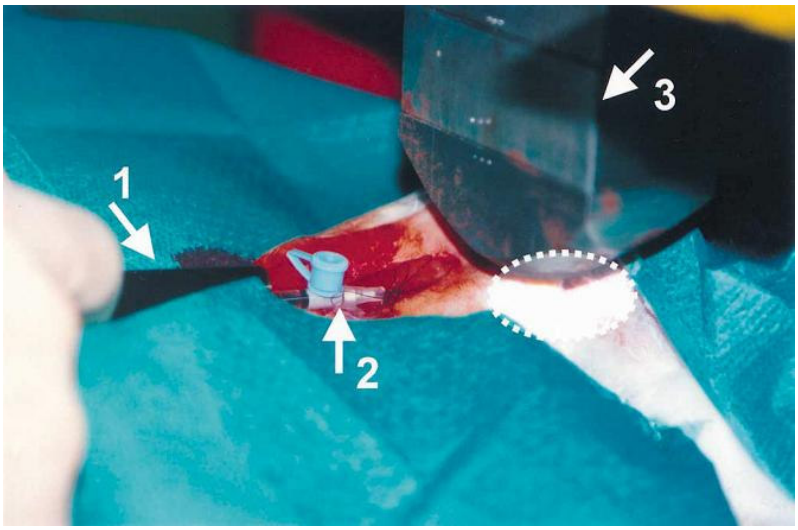

Figure 1.7: Magnetic drug delivery: Ferrofluid (1) is injected via a syringe (2) where particles are localized on tumor (dotted area) by an external magnet (3) [11].

Ferrofluids that contain cobalt and platinum compounds are also used in different applications such as in audio devices, inertia dampers, stepper motors, sensors and high-density digital storage [21].

1.3 Magnetic particle synthesis

Advancement in the use of magnetic nanoparticles for biomedical applications does require the synthesis of nanoparticles with better control of the size in narrow size distribution, high saturation magnetization, functional surfaces and resistance to agglomeration. Typical is the synthesis of bare iron oxide particles and then coating the selected size fraction with a suitable organic material for the selected applications, which is again followed by size selection steps. A major problem is the tendency of nanoparticles to

agglomerate due to their high surface to volume ratio. Addition of materials that can pacify the surface allows a certain control in agglomeration problem of the bare magnetic nanoparticles.

There are several synthetic methods for iron oxide nanoparticles such as micro-emulsion, sol-gel, bulk solution and gas deposition [22]. These methods offer the advantage of narrow size distribution, high magnetization values and high production rate besides many disadvantages such as uncontrolled oxidation of magnetite to maghemite and difficulty in removal of surfactants. Hyeon and co-workers reported the most successful synthesis of highly crystalline and monodisperse γ-Fe_2O_3 nanoparticles via thermal decomposition of iron pentacarbonyl in the presence of oleic acid at 100 ^oC and high temperature aging (300 ^oC) [23]. Problems with this approach are maghemite has lower saturation magnetization than magnetite; nanoparticles need to be removed from high boiling solvents and transferred into water which requires the exchange of hydrocarbon ligands from the iron oxide surface with water soluble ones.

For the preparation of aqueous suspensions, one of the commonly used synthetic methods is the co-precipitation of Fe^{2+} and Fe^{3+} salts by addition of a base in aqueous media but size distribution of the magnetic cores are not as narrow as the organic preparations [22]. The control of size and composition of nanoparticles depends on the type of salts used and some reaction conditions like Fe^{2+} and Fe^{3+} ratio, temperature, pH and ionic strength of the media. Yet, there is no detailed systematic study of the reaction variables for the control of particle size and properties. Iron oxide nanoparticles are usually coated with organic or inorganic molecules in inert atmosphere to prevent the oxidation and agglomeration. Bubbling nitrogen gas through the solution protects critical oxidation of the magnetite while reducing the particle size when compared with methods under air [24,25]. Adsorption of stabilizing agents on the surface of particles after synthesis or preparing magnetic fluids using anionic or cationic surfactants as dispersing agents are the commonly

used methods for particle stabilization. The change in nature of counterions and pH of the suspensions provided electrostatic stabilization to the charged magnetic nanoparticles. In addition, coating the particle surfaces with organic surfactants provides steric repulsion.

Polymeric stabilizers are effective in preventing particle aggregation. Polymeric coatings offer various functional groups on the surface of magnetic nanoparticles that can be useful for applications. Poly (vinyl alcohol) (PVA), poly (N-vinylpyrollidone) (PVP), poly (N-isopropylacrylamide) (PNIPAA) and poly (ethylene glycol) (PEG) are the commonly used coating materials for in vivo applications Poly (acrylic acid) was also reported as a polymeric stabilizer for iron oxide nanoparticles providing both electrostatic and steric repulsion against particle aggregation [26,27,28].

1.4 Purpose of the research

The overall objective of this project is to prepare functional SPIOs that are resistant to agglomeration in controlled size with a simple process that is preferably cost-effective as well. Such particles in small sizes (150-50nm) and in ultrasmall sizes (≤50nm) are desired for imaging and molecular targeting of agents and drugs in the diagnostic and therapy. Since particle size is crucial for each application, a statistical approach to predict particle size by controlling reaction parameters was also reported by Rondinone and his co-workers [29].

In order to achieve this, here, we primarily focused on the in situ coating of the iron oxide nanoparticles with polyacrylic acid to prevent aggregation during synthesis and control crystal size and size distribution. This was achieved by treating iron salts with ammonium hydroxide in water in the presence of PAA. There are number of variables that may control the particle size (core and hydrodynamic), size distribution, magnetic characteristics and stability (resistance to agglomeration). PAA molecular weight, iron and

base concentrations and (COOH)/iron mole ratio are the four factors chosen to control these responses. The aim of this research is to determine the most effective factors determining primarily the hydrodynamic particle size and find a general mathematical equation that predicts size using these effective factors. Also, we are interested in identifying the factors effective on particle stabilization and magnetization. Design Expert 7.0 and Minitab14 Release statistical programs, two-level full factorial design was used to determine best set of experiments and find the possible correlations between these four factors and responses. Such systematic study would draft some basic rules in the size control of nanoparticles in aqueous synthesis that may be transferable to other coating systems.

In our study, PAA sodium salt (Figure 1.8) was chosen as the coating material for the following reasons:

- provide multiple functional groups (carboxylic acid) for adsorption to the crystal surface
- provide electrostatic and steric stabilization
- provide functional surface (carboxylic acids) to the coated particles
- provide pH responsiveness

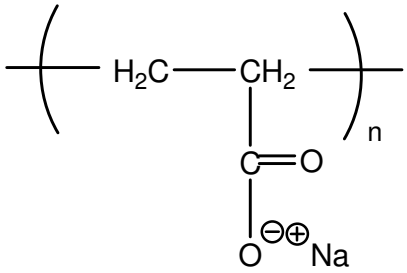

Figure 1.8: Chemical structure of poly (acrylic acid) sodium salt.

The second part of this project was to prepare stable (resistant to agglomeration) small and ultrasmall SPIOs with surface functionalities for applications in therapy and imaging. Size dependent uptake of the particles by the cells, investigation of site specific delivery of the particles and contrast enhancement capacity are within the ultimate scope of this project. First time, PAA coated nanoparticles of same type differing in only size will be systematically studied for cell uptake, targeted delivery and contrast behavior. Intracellular uptake of nanoparticles will be tested in cancer cell lines (HeLa and MCF7) and mouse macrophage (RAW 264.7). PAA-stabilized iron oxide nanoparticles with different particle sizes (30, 70 and 110nm) were conjugated with folic acid for the recognition by folate receptors as a model. Folate receptors are glycosylphosphatidylinositol-anchored, folate-binding proteins that are overexpressed in malignant tissues rather than the healthy ones. In this process, folate functionalized SPIOs would be recognized by the folate receptors on tumor cells and internalized via receptor-mediated endocytosis. (Due to the difficulty in finding and reproducing cell lines, this part is not completed by the time of the thesis defense. Cytotoxicity of the particles were tested by MTT assay. In order to evaluate the contrast enhancement behavior of our SPIOs, signal intensities of the aqueous suspensions of selected particle sizes were measured in clinical MRI and compared with commercial contrast agent Endorem®.

Chapter 2

EXPERIMENTAL PART

2.1 Materials

$FeCl_3.6H_2O$ and $FeCl_2.4H_2O$ were used as purchased from Fluka. Ammonium hydroxide (26% NH_3 in water, w/w) was purchased from Riedel-de Haen and used as supplied. Two different molecular weights (Mw ~ 5,100 and Mw~15,000 g/mol) of polyacrylic acid sodium salt were purchased from Aldrich. Milli-Q water was used for all preparations and work-up.

2.2 Synthesis of poly (acrylic acid) coated iron oxide nanoparticles

The following procedure was performed for all experiments:

PAA sodium salt was dissolved in required amount of water, transferred into a 100ml three necked round bottomed flask fitted with a mechanical stirrer, condenser and nitrogen inlet. After the polymer solution was deoxygenated for 30 minutes, iron salts (Fe^{3+} / Fe^{2+} mole ratio of 2) were added to the flask and stirred at 400rpm under nitrogen for about 15 min. Reaction flask placed into an oil bath at 85 ^{o}C. After 10min of mixing, ammonium hydroxide was injected to the flask with vigorous stirring at 800rpm and reaction allowed to continue for 30 minutes (*).

$$Fe^{2+} + 2Fe^{3+} + 8OH^- \rightarrow Fe(OH)_2 + 2Fe(OH)_3$$
$$\rightarrow Fe_3O_4 + H_2O \quad (*)$$

After the colloidal suspension cooled to room temperature, it was transferred to a glass bottle and sit atop a handheld magnet (0.3 Tesla) overnight. pH of all experiments was measured the next day. Any precipitate that might occur was removed. 50% of the colloidal solution was washed with water using ultrafiltration device (MwCo 5,000 g/mol, 15,000 g/mol) till pH 7-8. All solutions were filtered from 450 nm and 100 nm filters after synthesis and ultrafiltration, respectively.

PAA molecular weight, iron and base concentrations and (COOH)/iron mole ratio are the reaction factors and the ranges for each are given in Table 2.1. These ranges were chosen based on our previous trials and literature values.

Factors	Low	High
Fe conc.[a]	0.03	0.3
Reactive/Fe[b]	0.3	4
Base ratio[c]	1	3
Mw of PAA[d]	5100	15000

Table 2.1: Reaction variables

a Total iron concentration (M): (mole Fe (II) + mole Fe (III))/Volume

b Reactive/Fe: mole COONa/ mole Fe

c Base ratio: mole base/ [COONa mole + (2.5 mole Fe)]

d Molecular weight of PAA: g/mol

Twenty experiments were created by the statistical programs (Design Expert 7.0 and Minitab 14 Release) based on four factor two-level full factorial design with two center points per block within the given range of each variable (Table 2.2). PAA molecular weight is a categorical factor and we had two blocks for two molecular weights.

2.3 Characterization methods

Hydrodynamic size (D_h) of PAA-coated iron oxide nanoparticles were measured by Malvern Zetasizer Dynamic Light Scattering (DLS). Hydrodynamic sizes of particles were measured both before and after washing off excess polymer via ultrafiltration. Reported sizes are 1/100 dilution of original reaction concentrations (stock solution) in order to eliminate the viscosity effect on particle size measurements. Unless indicated all sizes are measured without any size separation process such as filtration. Zeta potentials were measured by Brookhaven ZetaPals Zeta Potential Analyzer and viscosity of solutions were measured by Anton Paar Microviscometer. X-ray diffraction measurements with monochromatic CuKα radiation were taken to investigate the crystal structure of the particles on a X-Ray Powder Diffractometer (Huber, Guinier System 642). Aqueous solutions were dried on C-coated Cu grid and used for Transmission Electron Microscopy (TEM) images and Scanning Electron Microscopy (SEM LEO Supra 35 VP) analysis. The magnetization of the dried particles was measured by Vibrating Sample Magnetometer (VSM) and iron concentration determination was performed by Inductively Coupled Plasma analysis on a SPECTRO GENESIS EOP ICP. Thermogravimetric Analysis (Shimadzu TGA 50H) was performed for iron oxide nanoparticles. IR measurements (Nicolet FTIR) were performed by preparing KBr pellets of dried powders.

Sample ID	Fe conc. (M)	Reactive/Fe (mol/mol)	Base ratio	Mw of PAA (g/mol)
MD33	0.03	4	1	5100
MD28	0.03	4	3	15000
MD29	0.3	4	3	5100
MD25	0.165	2.15	2	15000
MD31	0.3	0.3	1	5100
MD32	0.03	0.3	1	15000
MD27	0.3	0.3	3	15000
MD30	0.3	4	1	15000
MD15	0.165	2.15	2	5100
MD26	0.03	0.3	3	5100
MD22	0.03	4	1	15000
MD20	0.03	0.3	1	5100
MD25R	0.165	2.15	2	15000
MD18RR	0.3	0.3	1	15000
MD17R	0.03	0.3	3	15000
MD23R	0.3	4	1	5100
MD15R	0.165	2.15	2	5100
MD21R	0.3	0.3	3	5100
MD19RR	0.3	4	3	15000
MD24	0.03	4	3	5100

Table 2.2: Design space obtained from Design Expert 7.0, two-level full factorial design.

Chapter 3

EXPERIMENTAL RESULTS & CHARACTERIZATION

3.1 Particle size and size distribution

Controlling particle size and preventing aggregation between particles have received considerable attention with the increasing need of applications for well-dispersed magnetic nanoparticles with uniform size, uniform physical and chemical properties. There are two different particle sizes that determine properties: Crystal size of the magnetic core and the hydrodynamic size.

Hydrodynamic size of particles was measured with Dynamic Light Scattering (DLS). This technique is used for measuring particle size over the size range of few nanometers to a few microns. The concept uses the idea of "Brownian Motion" that is based on the movement of particles in a resting fluid. In DLS measurements the speed of movement is used to calculate the particle size. Larger particles move slower than the smaller ones if the temperature and viscosity is the same. Hydrodynamic size is also a good measure for the detection of aggregation.

Initially, hydrodynamic size of stock solutions were measured after simple magnetic decantation procedure a three day rest atop a 0.3T magnet, meaning no size fractionation is attempted (Table 3.1).

In case of iron concentration, smaller particle sizes were observed with dilute solutions while concentrated solutions resulted in larger hydrodynamic size (Figure 3.1).

Sample ID	Fe conc. (M)	Reactive/Fe (mol/mol)	Base ratio (mol/mol)	Mw of PAA (g/mol)	Dh(I) unwsh (nm)	Dh(N) unwsh (nm)	Dh(I) wsh (nm)	Dh(N) wsh (nm)
MD33	0.03	4	1	5100	7	4	4	3
MD28	0.03	4	3	15000	28	16	59	44
MD29	0.3	4	3	5100	51	21	190	7
MD25	0.165	2.15	2	15000	164	10	*	*
MD31	0.3	0.3	1	5100	91	18	79	14
MD32	0.03	0.3	1	15000	142	16	142	24
MD27	0.3	0.3	3	15000	190	44	220	28
MD30	0.3	4	1	15000	220	16	*	*
MD15	0.165	2.15	2	5100	40	16	40	24
MD26	0.03	0.3	3	5100	122	28	79	16
MD22	0.03	4	1	15000	14	3	18	10
MD20	0.03	0.3	1	5100	91	38	79	14
MD25R	0.165	2.15	2	15000	79	40	91	38
MD18RR	0.3	0.3	1	15000	220	16	91	28
MD17R	0.03	0.3	3	15000	105	16	105	38
MD23R	0.3	4	1	5100	80	38	122	68
MD15R	0.165	2.15	2	5100	60	32	91	21
MD21R	0.3	0.3	3	5100	140	59	91	18
MD19RR	0.3	4	3	15000	150	21	*	*
MD24	0.03	4	3	5100	16	9	24	12

Table 3.1: Hydrodynamic size of particles : *Particles precipitated

Dh (I) unwsh: Intensity size distribution after synthesis.

Dh (I) wsh: Intensity size distribution after the removal of excess coating material.

Dh (N) unwsh: Number intensity distribution after synthesis.

Dh (N) wsh: Number intensity distribution after the removal of excess coating material.

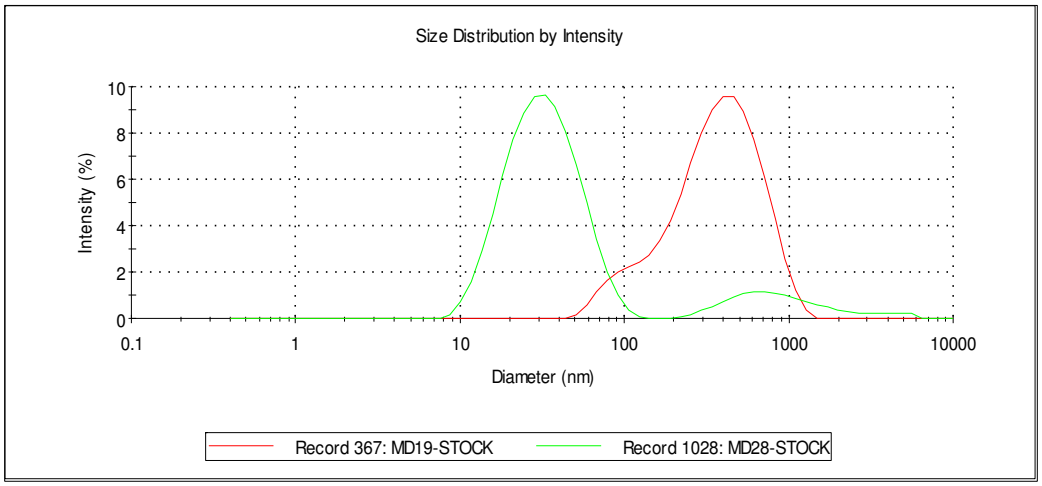

Figure 3.1: Effect of [Fe] under same conditions: 0.03 M (green) and 0.3 M (red).

Reactive/Fe ratio seems to be effective on hydrodynamic size, however no net correlation was found without statistical evaluations. Based on DLS data, hydrodynamic size mostly decreases with increasing reactive/Fe ratio suggesting a possibility of two or three way interaction between variables (Figure 3.2).

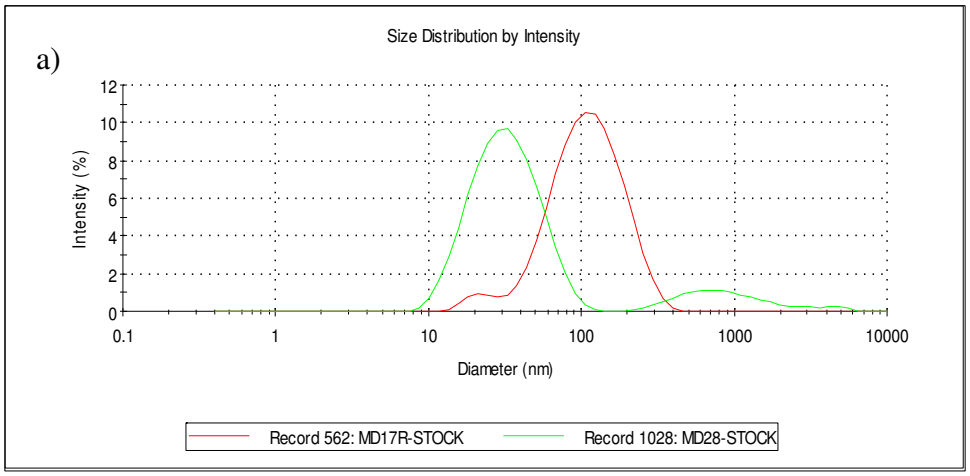

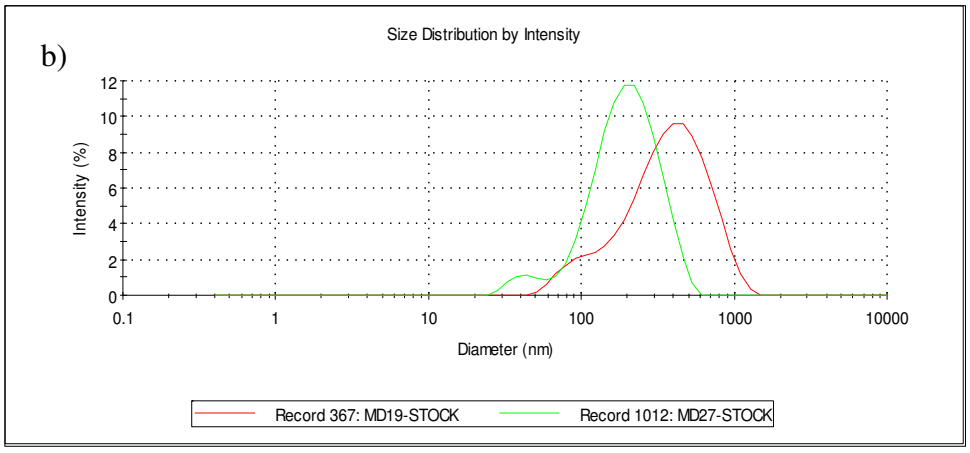

Figure 3.2: Two different measurements based on Reactive/Fe under same conditions.
a) 0.3 (red) and 4 (green),
b) 0.3 (green) and 4 (red).

Base ratio did not show a dramatic effect on particle size but in practice size distribution tends to broaden with decreasing base amount (Figure 3.3).

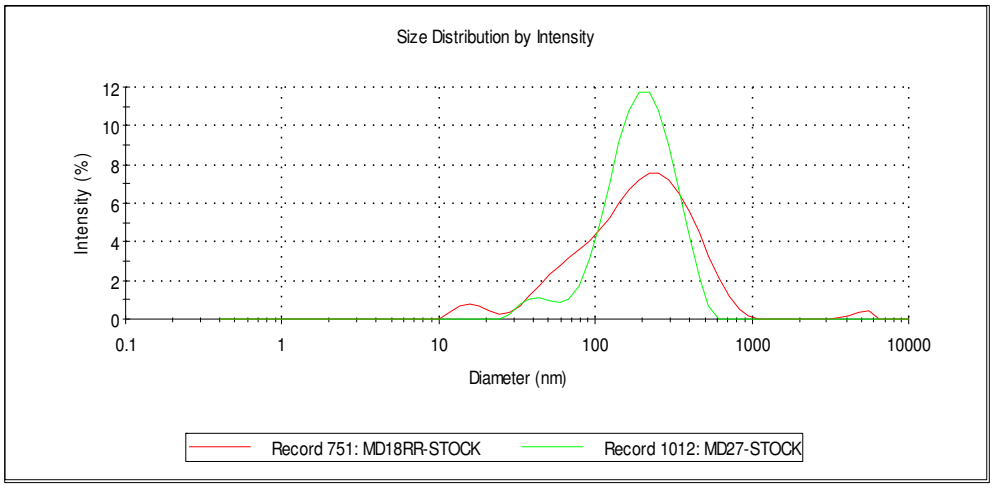

Figure 3.3: Effect of base ratio under same conditions: 1 (red) and 3 (green).

Molecular weight of polymer was the last factor affecting particle size. Although no significant difference was observed from DLS data (Figure 3.4) directly, larger hydrodynamic size was obtained with high Mw of PAA which confirms the statistical evaluations in Chapter 4.

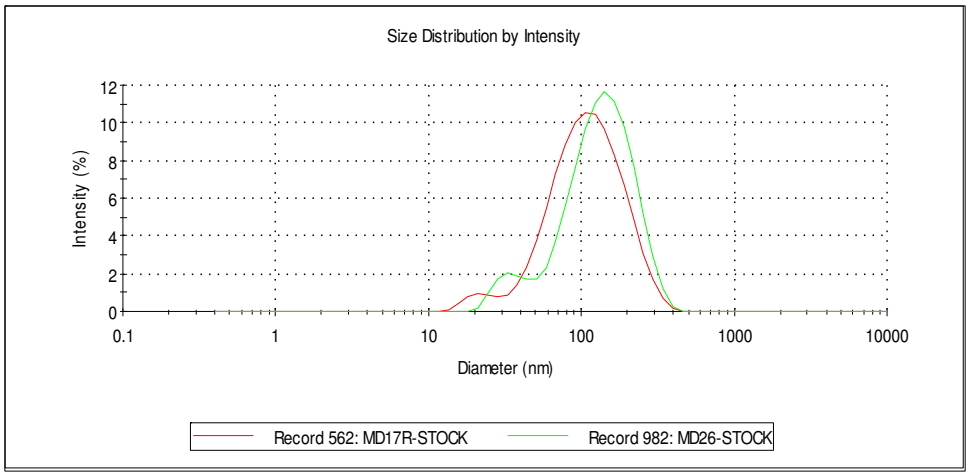

Figure 3.4: Effect of PAA molecular weight under same conditions: 5100g/mol (green) and 15000 g/mol (red).

3.2 Resistance to agglomeration

Stabilization of magnetic nanoparticles can be achieved by coating the surfaces with polymeric materials. Poly (acrylic acid) sodium salt was used as a polymeric stabilizer in all experiments providing both electrostatic and steric repulsion against particle aggregation. Carboxylic acid groups offer multiple adsorption sites on the iron oxide core

while other free groups provide water solubility and surface functionality to the particle. These free carboxylic acid groups on the surface also maintain electrostatic repulsion that prevents aggregation (Figure 3.5). The stability of the polymer coating on the surface of iron oxide core is very important for particles to resist agglomeration. In our study, stability upon dilution and stability after removal of excess coating material were tested for all reactions. Long-term stability was another important quality to follow in all experiments. Particles which precipitated in 3 days (based on practical observation) were evaluated as unstable (Table 3.2).

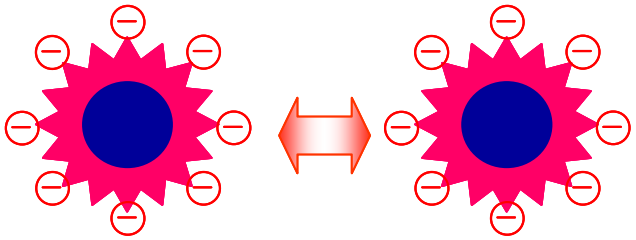

Figure 3.5: Electrostatic stabilization of particles.

Sample ID	Fe conc. (M)	Reactive/Fe (mol/mol)	Base ratio (mol/mol)	Mw of PAA (g/mol)	St. unwsh	St. uo to 1/10000 wsh	St. up to 1/1000 wsh	Long term st.	Magn
MD33	0.03	4	1	5100	0	0	0	1	0
MD28	0.03	4	3	15000	0	0	0	1	0
MD29	0.3	4	3	5100	1	1	1	0	1
MD25	0.165	2.15	2	15000	1	0	0	0	1
MD31	0.3	0.3	1	5100	1	0	1	1	1
MD32	0.03	0.3	1	15000	1	0	1	1	1
MD27	0.3	0.3	3	15000	1	1	1	0	1
MD30	0.3	4	1	15000	0	0	0	0	1
MD15	0.165	2.15	2	5100	1	1	1	1	1
MD26	0.03	0.3	3	5100	1	0	1	1	1
MD22	0.03	4	1	15000	0	0	0	1	0
MD20	0.03	0.3	1	5100	0	0	1	1	1
MD25R	0.165	2.15	2	15000	1	0	1	0	1
MD18RR	0.3	0.3	1	15000	1	1	1	0	1
MD17R	0.03	0.3	3	15000	1	1	1	1	1
MD23R	0.3	4	1	5100	1	1	1	0	1
MD15R	0.165	2.15	2	5100	1	1	1	0	1
MD21R	0.3	0.3	3	5100	1	1	1	1	1
MD19RR	0.3	4	3	15000	0	0	0	0	1
MD24	0.03	4	3	5100	0	0	1	1	1

Table 3.2: Stability and magnetization of particles:
0: unstable/non-magnetic, 1: stable/magnetic.

Particles within the same size range after dilutions up to 1/10,000 were evaluated as stable (Figure 3.6a). If particles do not precipitate but size increases then it is evaluated as unstable as well (Figure 3.6b).

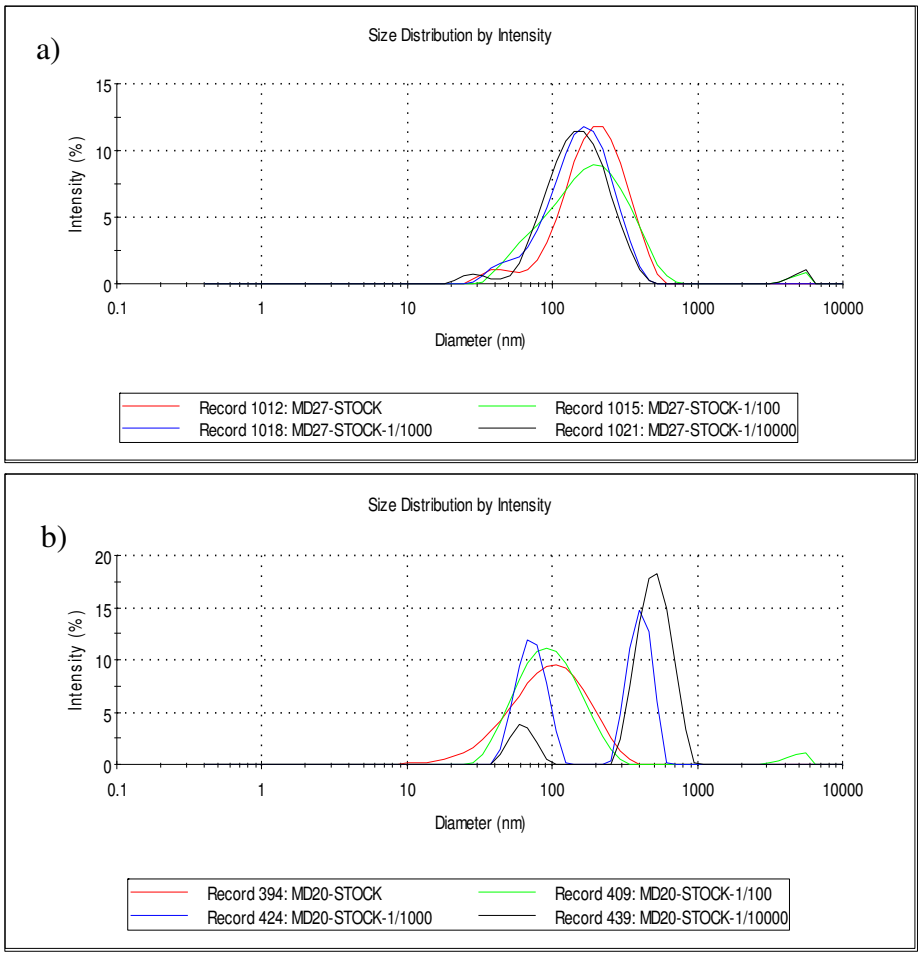

Figure 3.6: Stability upon dilution of unwashed particles: a) stable, b) unstable. Stock solution (red), 1/100 dilution (green), 1/1000 dilution (blue) and 1/10000 dilution (black).

Excess unbound polymer in stock solutions is removed via ultrafiltration with distilled water. This process allows us to test the stability of the nanoparticles in the absence of

excess coating material indicating the stability of polymer adhesion to the crystal surface. No dramatic size increase after ultrafiltration was evaluated as stable (Figure 3.7). If the coating is not stable, desorption will occur from particle surface and the particles will aggregate resulting in larger hydrodynamic size (Figure 3.8).

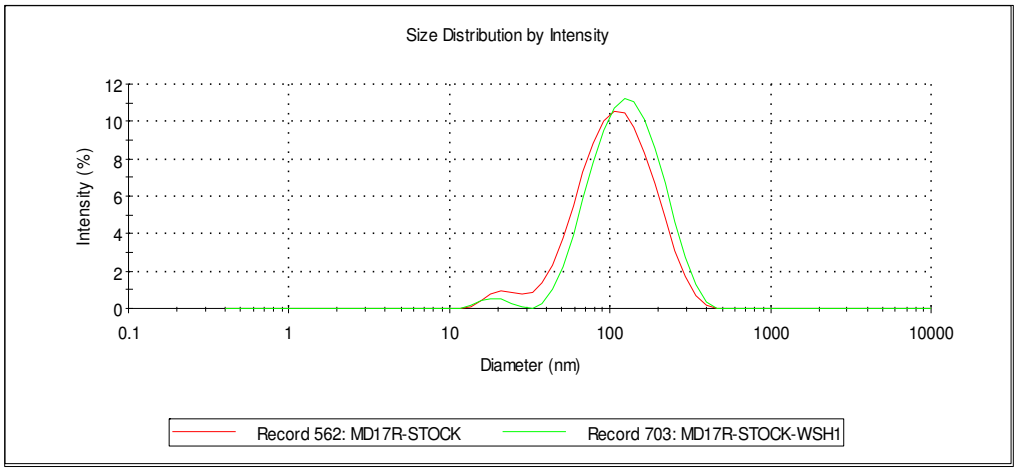

Figure 3.7: Effect of washing on particle size and stability:
Stock solution after synthesis (red) and after ultrafiltration (green).

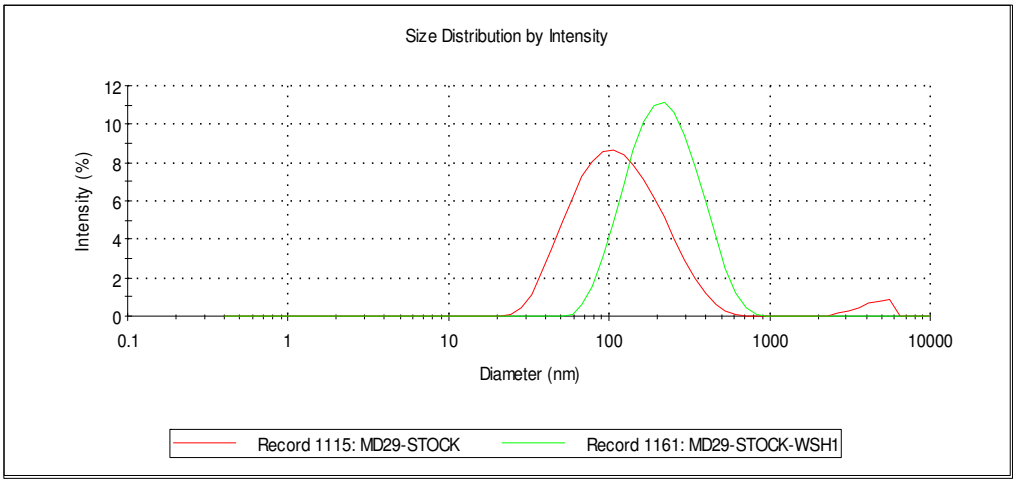

Figure 3.8: Effect of washing on particle size and instability:
Stock solution after synthesis (red) and after ultrafiltration (green).

Stability of the washed particles was also tested by dilution up to 1/10000. Stable and unstable particles were selected based on the same idea after synthesis (Figure 3.9).

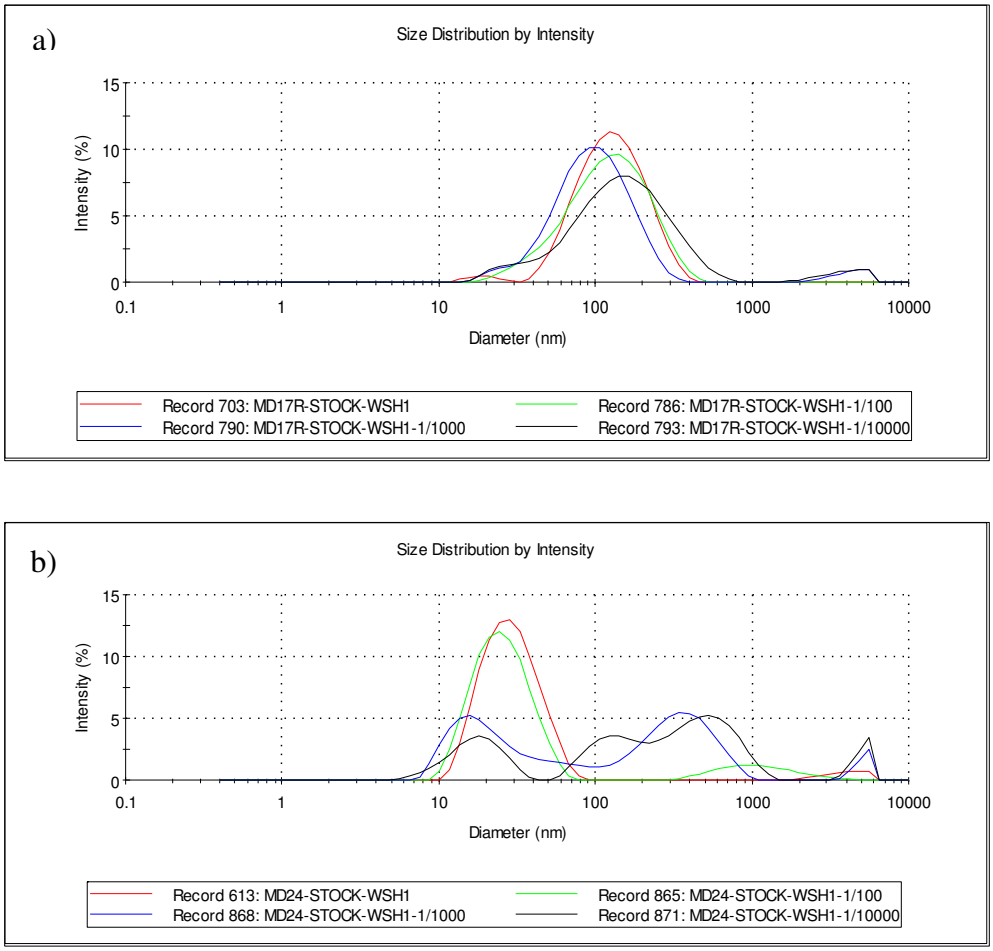

Figure 3.9: Stability upon dilution of washed particles: a) stable, b) unstable. Stock solution (red), 1/100 dilution (green), 1/1000 dilution (blue) and 1/10000 dilution (black).

.

Furthermore, all stock solutions were filtered from 450 nm and 100 nm filters after synthesis and after ultrafiltration with distilled water, respectively. This process was important for cell study where particle size is crucial for cellular uptake as explained in Chapter 1. Figure 3.10 displays the difference in hydrodynamic sizes after filtration.

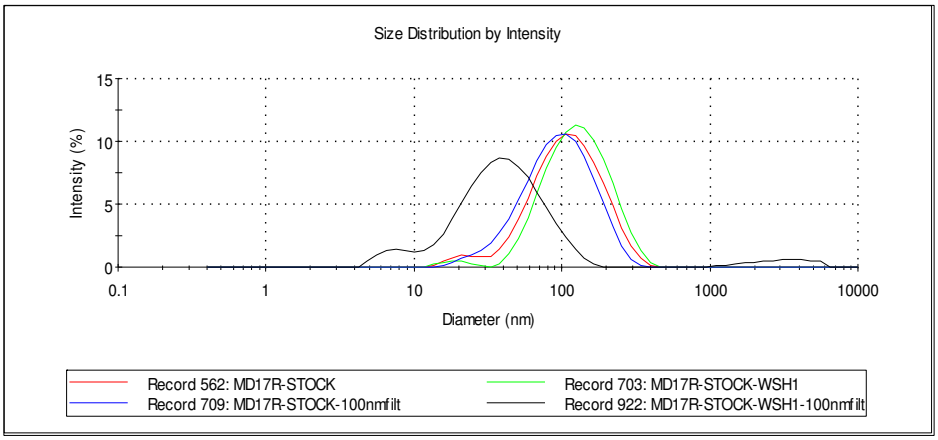

Figure 3.10: Hydrodynamic size of washed particles before (green) and after (black) being passed through 100 nm filter.

3.3 Viscosity effect

When the solution is too viscous, hydrodynamic size can be calculated larger than its normal value by DLS. This is well observed in some of the solutions, where the hydrodynamic size of the stock was larger than the size of the dilutions (Figure 3.11).

DLS calculates the hydrodynamic size based on the dynamic viscosity of distilled water which is 0.8862 mPa.s. Viscosity of stock solutions were measured around 1.1, while viscosity of the 1/100 dilution was about 0.88 mPa.s that is very close to distilled water

(Figure 3.12). Therefore, we used the size of 1/100 dilutions of all reactions in the statistical analysis. In addition, DLS data confirmed that the size of 1/100 dilutions would be more well-matched than the size of stock solutions (Figure 3.13).

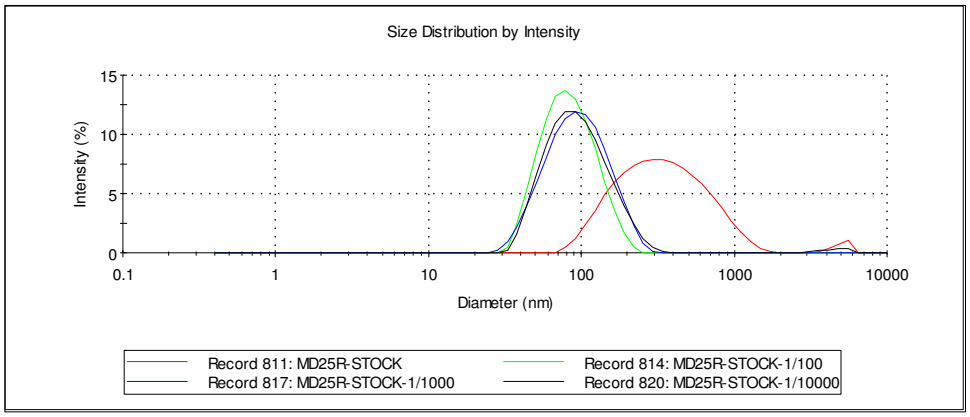

Figure 3.11: Hydrodynamic size of stock solution (red), 1/100 dilution (green), 1/1000 dilution (blue) and 1/10000 dilution (black).

MD35-STOCK - 05 Aralık 2005 Pazartesi, 17:04 (a)

Sample				AMVn	
Sample Name []	Angle [°]	sin(Angle) []	1/sin(Angle) []	Dyn. Viscosity [mPa.s]	Const. K1 [mPa.cm3/g]
stock	45.00	0.70711	1.41421	1.1136	0.01075
stock	45.00	0.70711	1.41421	1.1207	1.1207
stock	45.00	0.70711	1.41421	1.1135	0.01075
stock	45.00	0.70711	1.41421	1.1199	0.01075
stock	45.00	0.70711	1.41421	1.1169	0.01075

MD35-STOCK-1e100 - 05 Aralık 2005 Pazartesi, 16:23 (b)

Sample				AMVn	
Sample Name []	Angle [°]	sin(Angle) []	1/sin(Angle) []	Dyn. Viscosity [mPa.s]	Const. K1 [mPa.cm3/g]
1/100 dilution	45.00	0.70711	1.41421	0.8648	0.01075
1/100 dilution	45.00	0.70711	1.41421	0.8603	0.01075
1/100 dilution	45.00	0.70711	1.41421	0.8683	0.01075
1/100 dilution	45.00	0.70711	1.41421	0.8578	0.01075
1/100 dilution	45.00	0.70711	1.41421	0.8628	0.01075

Figure 3.12: Average dynamic viscosity a) stock solution, b) 1/100 dilution of stock solution.

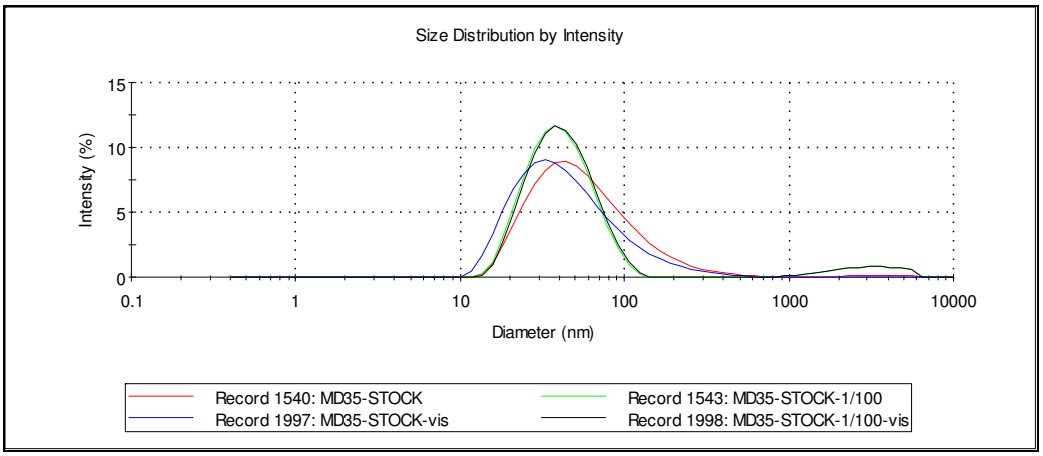

Figure 3.13: Stock solution before (red) and after viscosity correction (blue), 1/100 dilution of stock solution before (green) and after viscosity correction (black).

3.4 pH sensitivity

Polyacrylic acid is pH sensitive with isoelectric point at 2.4 [26]. As the ionization of the carboxylic acid groups increases stabilization due to electrostatic repulsion increases. At acidic pH where the carboxylic acid groups are protonated, electrostatic repulsion is replaced with attraction due to H-bonding and the particles begin to aggregate (Figure 3.14 and 3.15). Therefore below pH 4 particles precipitated out of solution. However, they can be redispersed by increasing pH. Also, isoelectric point of polyacrylic acid coated particles was determined. pH vs. Zeta potential graph showed that there is no net charge on particle surface at pH 2.4 which is in agreement with literature data (Figure 3.16) [26].

pH responsive nature of the particles can be exploited in drug unloading and diagnostic imaging since tumor cells tend to have lower pH than healthy ones .

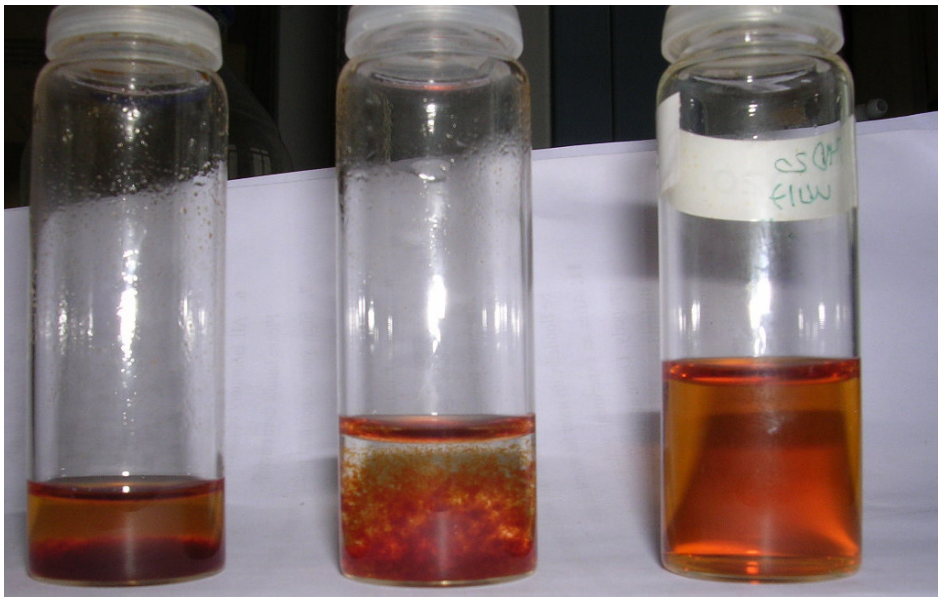

Figure 3.14: pH response of nanoparticles: From left to right: 2, 4, 7.

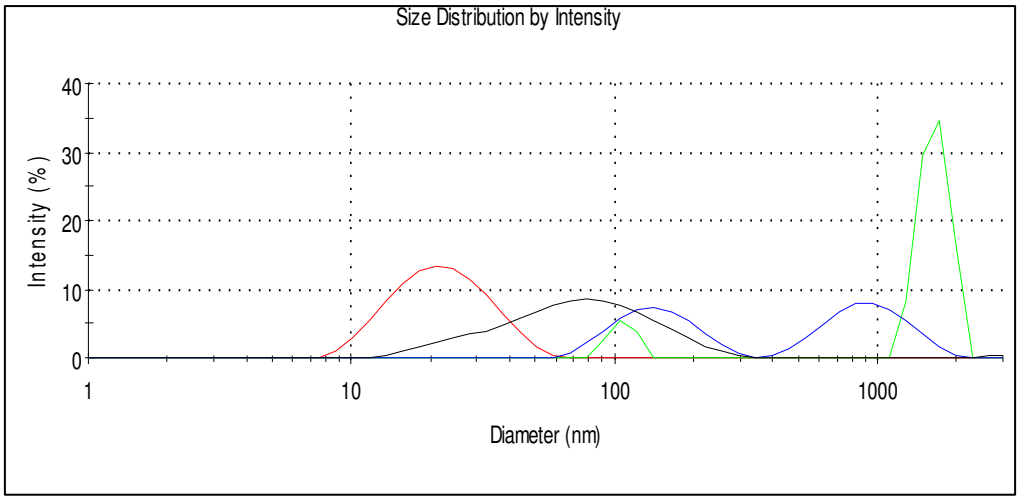

Figure 3.15: Particle size-pH relationship for MD24 after being washed and filtered from 100nm filter: pH 8.5 (red), pH 7 (black), pH 4 (blue), pH 2 (green).

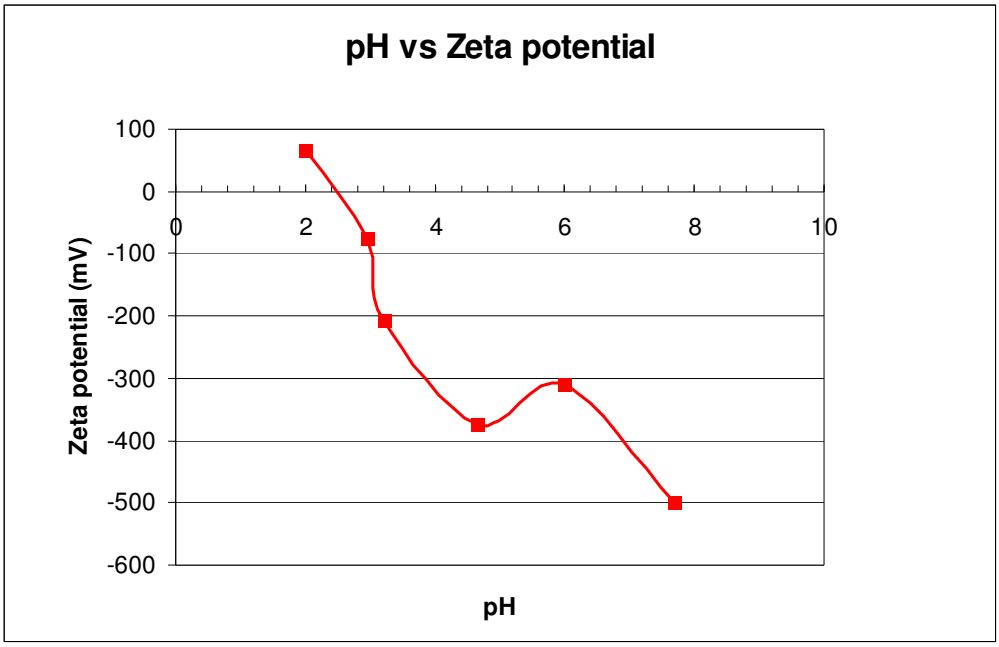

Figure 3.16: Isoelectric point of PAA.

3.5 XRD analysis

X-Ray Diffraction (XRD) technique was used to determine the size and composition of crystalline magnetic cores of the PAA-coated iron oxide nanoparticles. Every sample synthesized was analyzed with this technique to see the effect of reaction parameters on crystal growth and particle composition (Appendix A). To observe the PAA effect during iron oxide synthesis, poly (acrylic acid) sodium salt, bare iron oxide nanoparticles (in the absence of PAA) and PAA-stabilized iron oxide nanoparticles (after the removal of excess PAA) were analyzed (Figure 3.17).

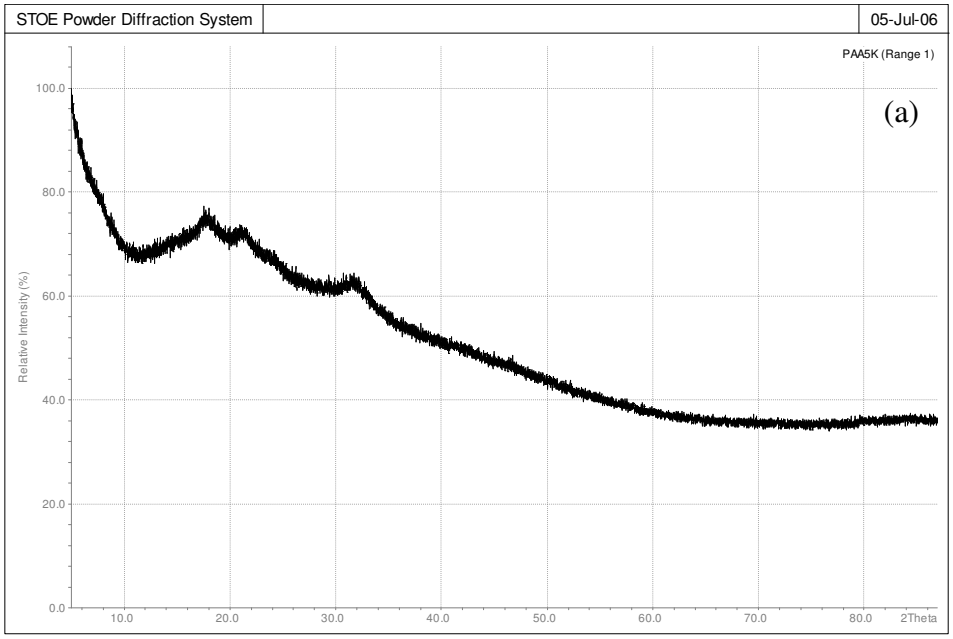
STOE Powder Diffraction System
05-Jul-06
PAA5K (Range 1)
(a)
Relative Intensity (%)
100.0
80.0
60.0
40.0
20.0
0.0
10.0
20.0
30.0
40.0
50.0
60.0
70.0
80.0
2Theta

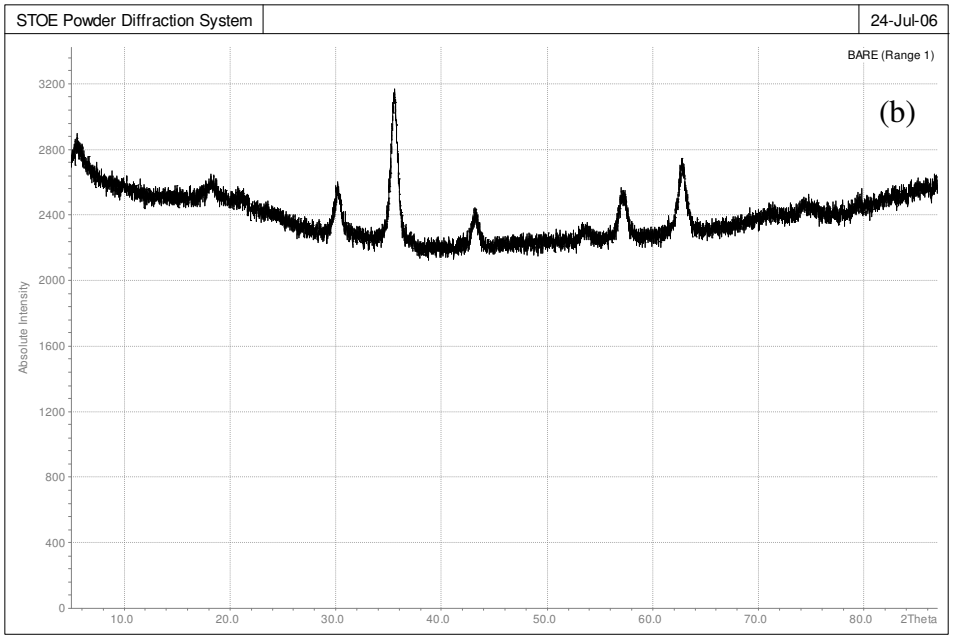
STOE Powder Diffraction System
24-Jul-06
BARE (Range 1)
(b)
Absolute Intensity
3200
2800
2400
2000
1600
1200
800
400
0
10.0
20.0
30.0
40.0
50.0
60.0
70.0
80.0
2Theta

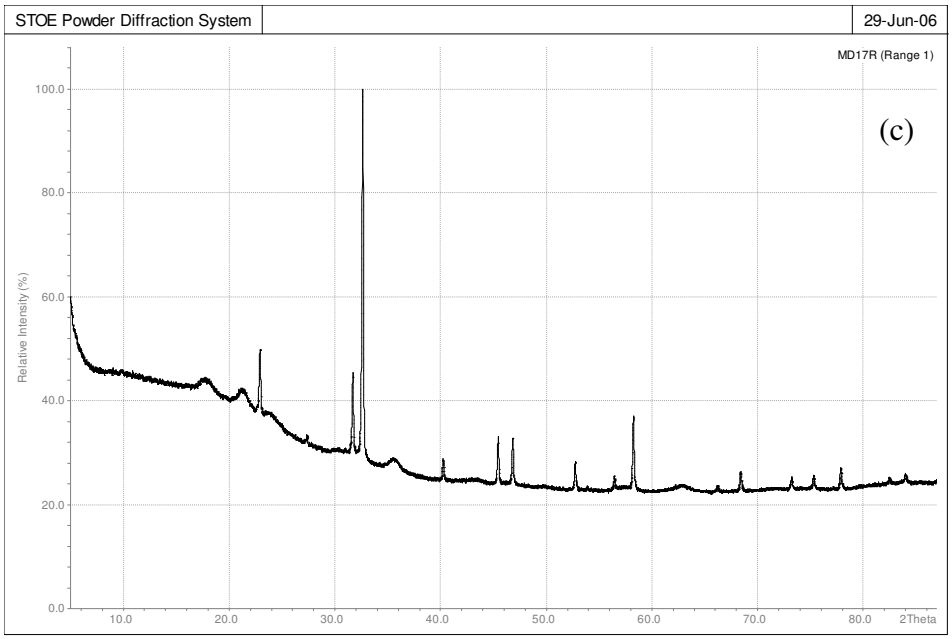

Figure 3.17: X-Ray diffraction diagram a) poly (acrylic acid) sodium salt, b) bare iron oxide nanoparticles, c) PAA-coated iron oxide nanoparticles (MD17R).

Iron oxide nanoparticles prepared in the absence of PAA show six diffraction peaks at $2\theta = 30.2^{\circ}$, 35.7°, 43.4°, 57.4°, and 62.9°, which are the characteristic peaks of standard Fe_3O_4 crystal. However, the additional diffraction peak at $2\theta = 32.8^{\circ}$ show that PAA-coated iron oxide nanoparticles also consist of γ–Fe_2O_3 crystals. Actually this has been seen in other systems [26]. This can be due to the acidic pH of PAA solution (pH 2.3) which would oxidize Fe^{2+} to Fe^{3+} forming Fe_2O_3, although Fe^{3+}/Fe^{2+} mole ratio was chosen 2 at the beginning of the reaction.

The major difference between the XRD diagrams of all experiments was found as Reactive/Fe ratio. When the Reactive/Fe ratio is larger, XRD diffraction peaks were not

intense. For non-magnetic materials, this result can be reasonable due to insufficient crystal growth. However, less intense peaks were also seen for magnetic materials which can be due to the formation of very small crystals in the presence of many polymer chains.

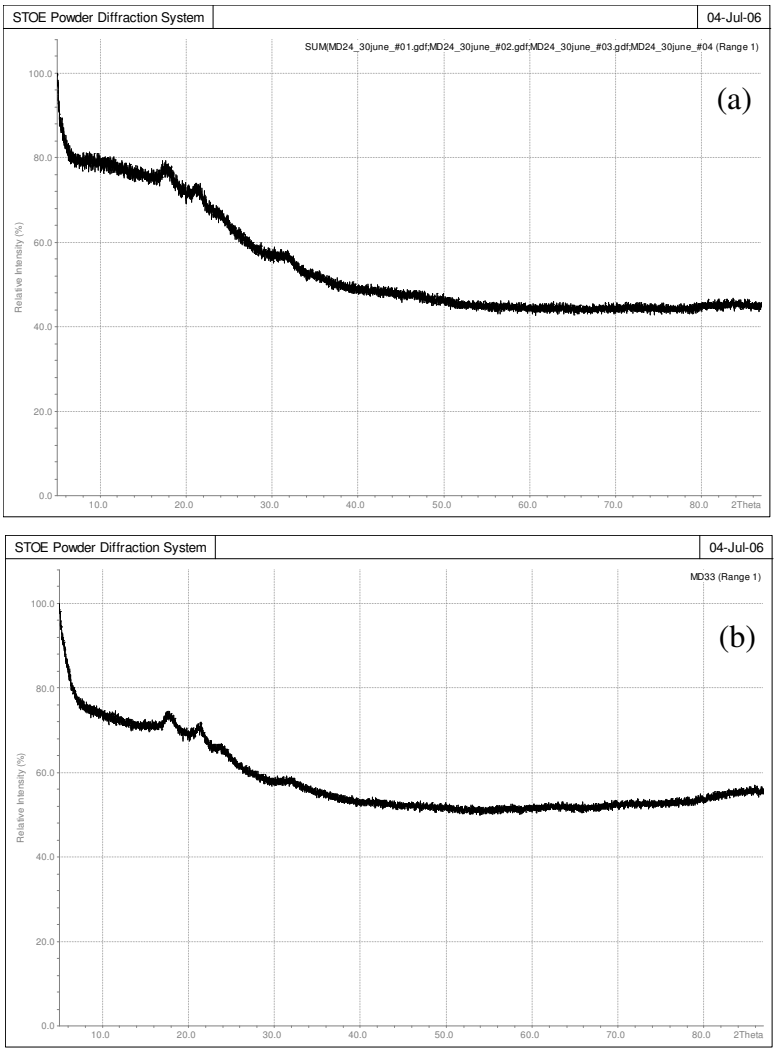

Figure 3.18: XRD diagrams of nanoparticles:
a) magnetic (MD24), b) non-magnetic (MD33).

In addition, the particle size of magnetite was calculated according to the Debye–Scherrer equation,

$$D = 0.9\lambda / \beta \cos \theta$$

where D is the average crystallite size (Å), λ is the wavelength of X-rays (CuKα: λ = 1.5418 Å), θ is the Bragg diffraction angle, and β is the full width at half maximum (FWHM) (in radians). By using the equation above and the FWHM of the diffraction peak at $2\theta = 35.65^{\circ}$, the crystallite size of the Fe_3O_4 in the presence of PAA was calculated as 5.2 nm, which was smaller than the crystallite size of bare Fe_3O_4 (6.5 nm) synthesized in the absence of PAA. This result also shows that the presence of PAA reduced the core size of Fe_3O_4 due to the fact that the carboxylic acid groups of PAA not only promoted nucleation but also inhibited growth of the Fe_3O_4 particles through surface passification. Core sizes were calculated for all experiments using both $2\theta = 35.7^{\circ}$ (Fe_3O_4) and $2\theta = 32.8^{\circ}$ (γ–Fe_2O_3) diffraction peaks (Table 3.3).

Sample ID	Fe conc. (M)	Reactive/ Fe (mol/mol)	Base ratio (mol/mol)	Mw of PAA (g/mol)	Dh(I) unwsh (nm)	Dh(N) unwsh (nm)	Dh(I) wsh (nm)	Dh(N) wsh (nm)	XRD Dc (Fe_3O_4)	XRD Dc (Fe_2O_3)
MD33	0.03	4	1	5100	7	4	4	3	-	-
MD28	0.03	4	3	15000	28	16	59	44	-	-
MD29	0.3	4	3	5100	51	21	190	7	6.11	6.21
MD25	0.165	2.15	2	15000	164	10	*	*	-	-
MD31	0.3	0.3	1	5100	91	18	79	14	3.44	-
MD32	0.03	0.3	1	15000	142	16	142	24	12.27	9.2
MD27	0.3	0.3	3	15000	190	44	220	28	-	-
MD30	0.3	4	1	15000	220	16	*	*	-	-
MD15	0.165	2.15	2	5100	40	16	40	24	-	-
MD26	0.03	0.3	3	5100	122	28	79	16	-	-
MD22	0.03	4	1	15000	14	3	18	10	-	-
MD20	0.03	0.3	1	5100	91	38	79	14	7.87	13.8
MD25R	0.165	2.15	2	15000	79	40	91	38	6.78	11.82
MD18RR	0.3	0.3	1	15000	220	16	91	28	6.87	-
MD17R	0.03	0.3	3	15000	105	16	105	38	5.2	10.35
MD23R	0.3	4	1	5100	80	38	122	68	8.49	13.34
MD15R	0.165	2.15	2	5100	60	32	91	21	6.47	41.3
MD21R	0.3	0.3	3	5100	140	59	91	18	-	-
MD19RR	0.3	4	3	15000	150	21	*	*	-	-
MD24	0.03	4	3	5100	16	9	24	12	-	3.56

Table 3.3. Reaction variables and particle size:

Dc (core size) was calculated for both compositions.

* particles precipitated

- less intense peaks

3.6 IR analysis

Fig. 3.19 shows a comparison between the IR spectra of the bare (Fe_3O_4) nanoparticles, pure PAA sodium salt, and the iron oxide nanoparticles synthesized in the presence of PAA. The atoms of Fe on the surface of Fe_3O_4 particles were expected to adsorb −OH and COO− groups of PAA, and the atoms of O on the particle surface would adsorb H^+. Also, the HO-rich surface of Fe_3O_4 nanoparticles could react with the carboxylic acid groups of PAA that remain in solution. Previously, it was reported that the characteristic absorption bands of the Fe–O bond of bulk Fe_3O_4 were at 570 and 375 cm−1 [30]. Although, transmission bands are not clearly seen at 500 cm^{-1}, IR spectrum of Fe_3O_4 nanoparticles exhibit a blue shift due to nanoscale dimensions and the characteristic transmission bands of the Fe–O bond were shifted to high wavenumbers of about 580 in Fig. 3.14. The IR spectrum of the PAA sodium salt shows peaks at 1570 and 1410 cm^{-1} that correspond to the COO^- antisymmetric vibration and the COO^- symmetric vibration. Same peaks were also observed for PAA-coated iron oxide nanoparticles which indicate the binding between carboxylate groups and Fe atoms with both oxygen atoms interacting with the metal on the surface [31,32].

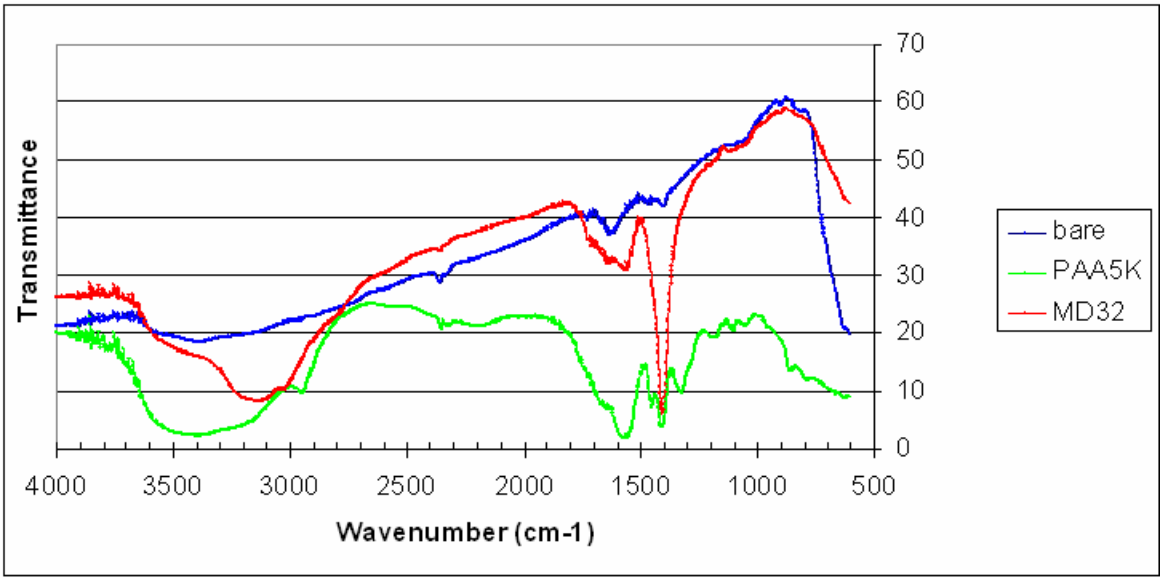

Figure 3.19: IR spectra of bare Fe_3O_4 nanoparticles, pure PAA sodium salt and iron oxide nanoparticles in the presence of PAA (MD32).

3.7 TGA analysis

Fig. 3.20 shows the TGA analysis of the bare Fe_3O_4 nanoparticles, the PAA sodium salt (Mw 5100 g/mol), and iron oxide nanoparticles synthesized in the presence of PAA after the removal of excess polymer. Bare Fe_3O_4 nanoparticles showed insignificant weight loss from 100 to 800 ˚C. The initial degradation stage (100-220 ◦C) of pure PAA sodium salt corresponds to the dehydration and decarboxylation of the carboxylic acid groups of the PAA, while the main degradation temperature of the PAA was near 430 ˚C [28].

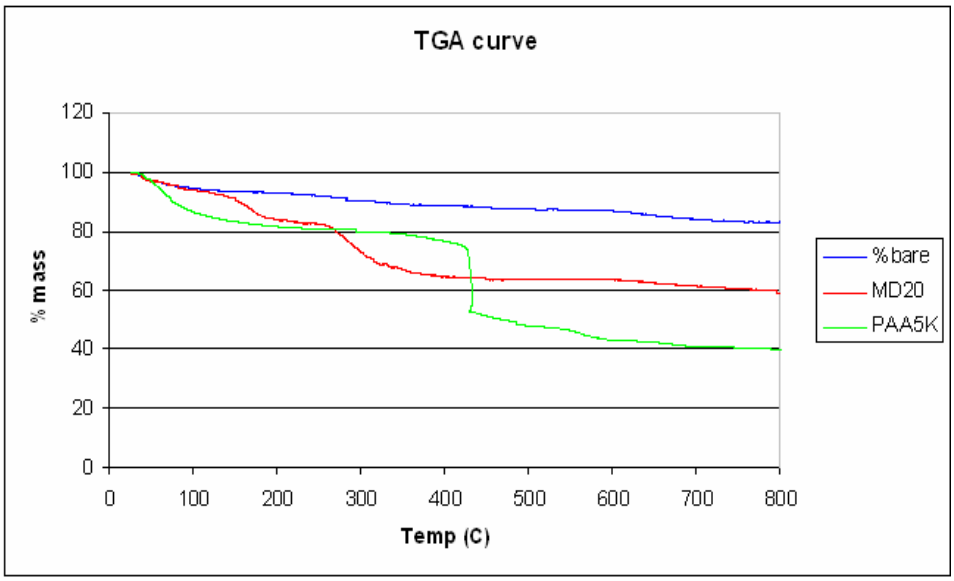

Figure 3.20: TGA curves for bare Fe_3O_4 nanoparticles, pure PAA sodium salt and iron oxide nanoparticles in the presence of PAA (MD20).

3.8 Electron microscopy analysis

Transmission electron microscope (TEM) was another characterization technique to observe the particle size, especially the core size, and morphology. The following figure display the TEM micrograph obtained for washed PAA-stabilized iron oxide nanoparticles (MD17R) (Figure 3.21). Although there were some large aggregates, core size was calculated around 8 nm (averaged over 7 particles) which is in between the sizes measured by XRD (5.2-10.35nm).

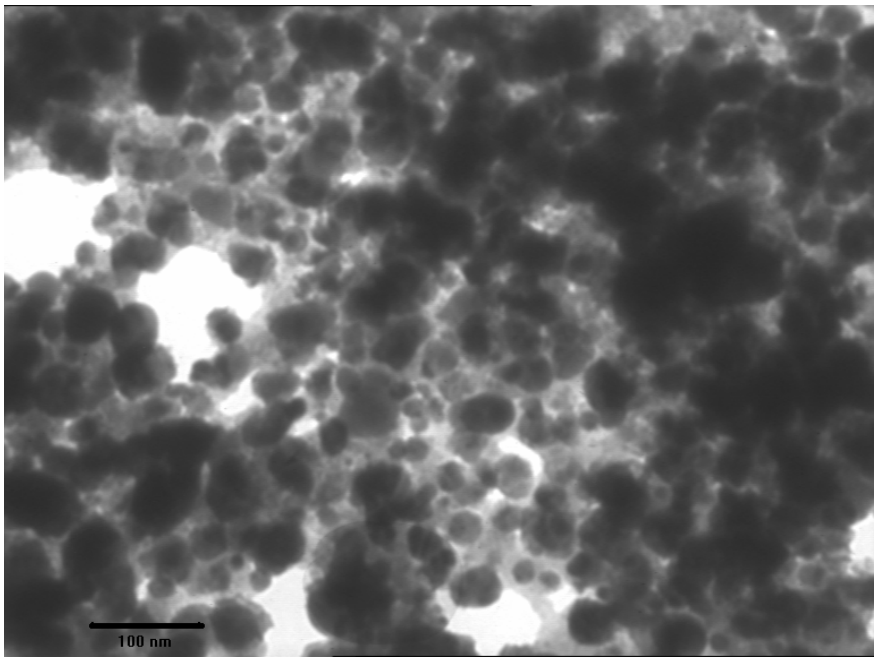

Figure 3.21: TEM micrograph of iron oxide nanoparticles synthesized in the presence of PAA (MD17R).

We analyzed MD17R also with SEM. We see some small particles that are made up of smaller ones around 50nm (Figure 3.22a) and also some larger crystalline structures of few hundred nanometers (Figure 3.22b)

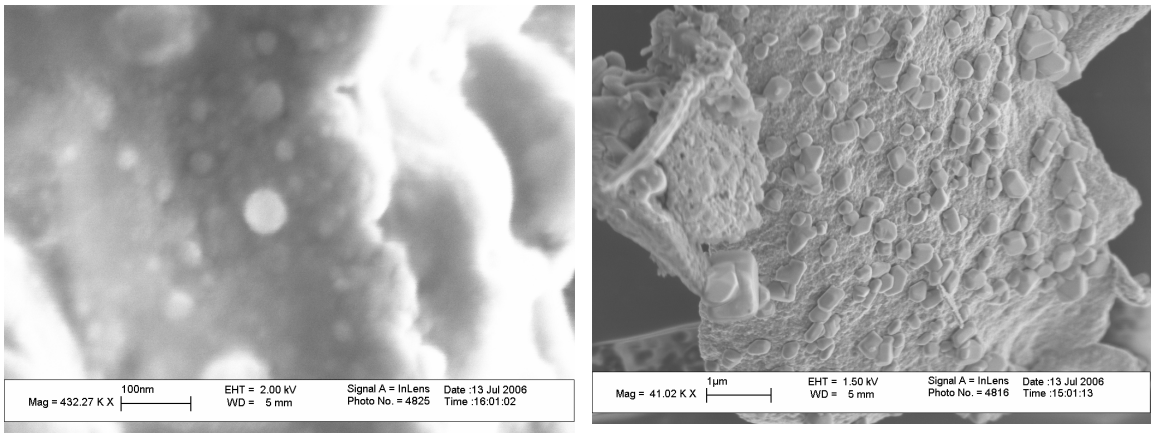

(a) (b)

Figure 3.22: SEM images of MD17R.

3.9 AFM analysis

Atomic force microscope (AFM) was used to observe particle size and size distribution. Hydrodynamic size of PAA-coated iron oxide nanoparticles (MD26 after excess polymer was removed) was around 100 nm with a size distribution of 10-400 nm according to intensity averaged results of DLS measurement (Figure 3.23). AFM images showed similar aggregate sizes confirming that the intensity based size measurement by DLS is a correct representation of these particles (Figure 3.24).

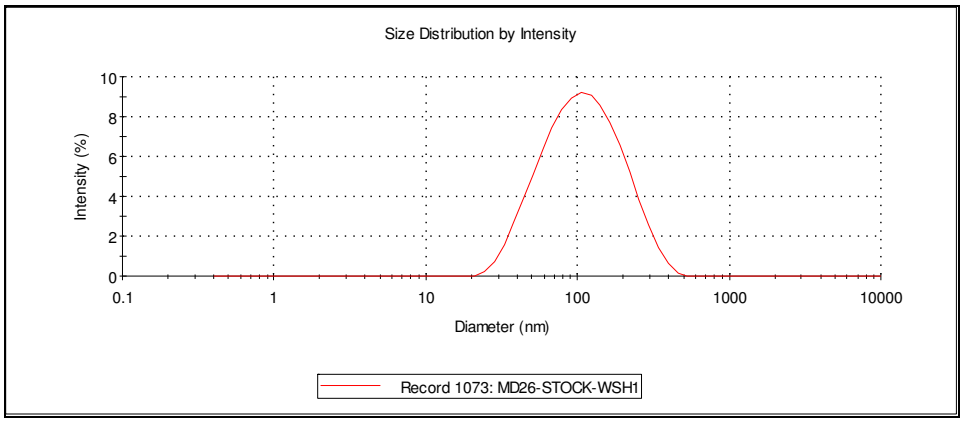

Figure 3.23: Hydrodynamic size of stock solution after ultrafiltration (MD26).

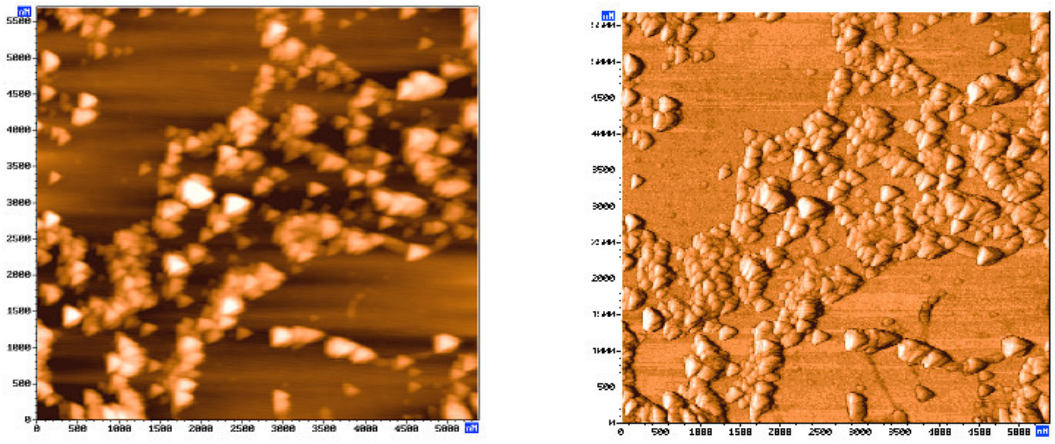

Figure 3.24: Height image (left) and phase image (right) of washed particles.

3.10 VSM data analysis

Vibrating Sample Magnetometer (VSM) systems are used to measure the magnetic properties of materials as a function of magnetic field, temperature, and time. In our study, this technique was used to create a hysteresis curve for PAA-coated iron oxide nanoparticles. The hysteresis curve was used to determine saturation magnetization (M_{sat}),

remanent magnetization (M_{rem}) and coercivity (H_c). According to this data, saturation magnetization (M_{sat}) was found as 10 emu/g for MD20 with no remanence and coercivity proving superparamagnetic behavior for nanoparticles (Figure 3.25).

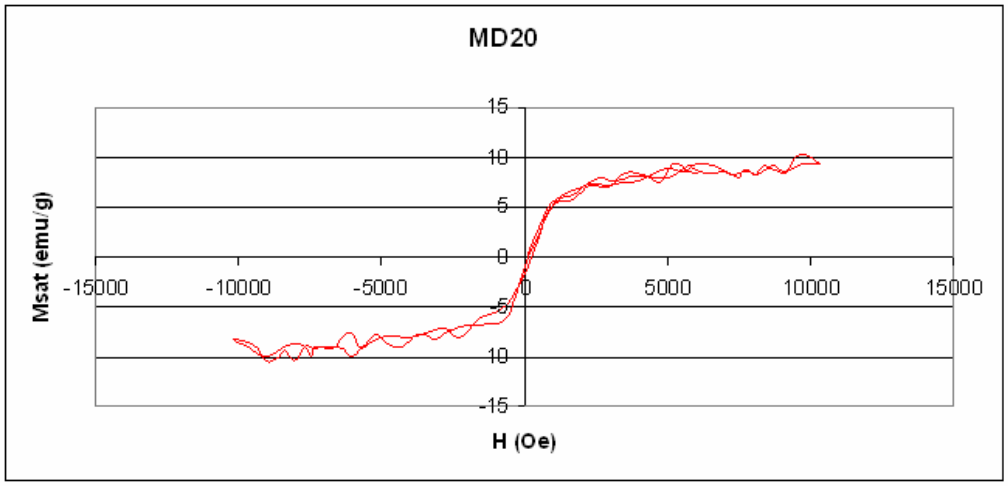

Figure 3.25: Hysteresis loop for PAA-coated iron oxide nanoparticles (MD20).

Similar curves with different M_{sat} values were obtained for the other samples. This data is quite noisy but it clearly shows the sign of superparamagnetism.

3.11 Other properties

Bimodality, intensity size distribution peak width and polydispersity index (for washed particles) were also evaluated to observe the effect of reaction parameters on these properties.

We have observed bimodal size distribution in the DLS data (only in the intensity distribution) with the high reactive/Fe ratio combined with low iron concentration (Table 3.4). This observation may be the result of micelle formation due to the presence of many polymeric chains at the high polymer concentration experiments, which is more dramatic in low Fe concentrations. In order to test this hypothesis, a sample solution was prepared only with poly (acrylic acid) sodium salt, ammonium hydroxide and distilled water in same concentrations with the reaction solution of which bimodal size distribution was observed. DLS measurements of both solutions confirmed that the second peak at larger size corresponds to the polymer micelle (Figure 3.26). In addition, it was observed that ultrafiltration with distilled water removed excess unbound polymer that has the ability to form micelles (Figure 3.27). It is important to note here that, because of this observation the first peak (smaller) that correspond to the core-shell nanoparticle was recorded as the hydrodynamic size of the resulting particles in the tables.

Sample ID	Fe conc. (M)	Reactive/Fe (mol/mol)	Base ratio (mol/mol)	Mw of PAA (g/mol)	bimodality
MD15R	0.165	2.15	2	5100	1
MD25R	0.165	2.15	2	15000	1
MD15	0.165	2.15	2	5100	1
MD21R	0.3	0.3	3	5100	1
MD30	0.3	4	1	15000	1
MD29	0.3	4	3	5100	1
MD23R	0.3	4	1	5100	1
MD32	0.03	0.3	1	15000	0
MD26	0.03	0.3	3	5100	0
MD20	0.03	0.3	1	5100	0
MD17R	0.03	0.3	3	15000	0
MD25	0.165	2.15	2	15000	0
MD31	0.3	0.3	1	5100	0
MD27	0.3	0.3	3	15000	0
MD18RR	0.3	0.3	1	15000	0
MD19	0.3	4	3	15000	0
MD33	0.03	4	1	5100	-1
MD22	0.03	4	1	15000	-1
MD28	0.03	4	3	15000	-1
MD24	0.03	4	3	5100	-1

Table 3.4: Reaction variables and bimodality: Bimodal:-1, shoulder: 0, monomodal: 1

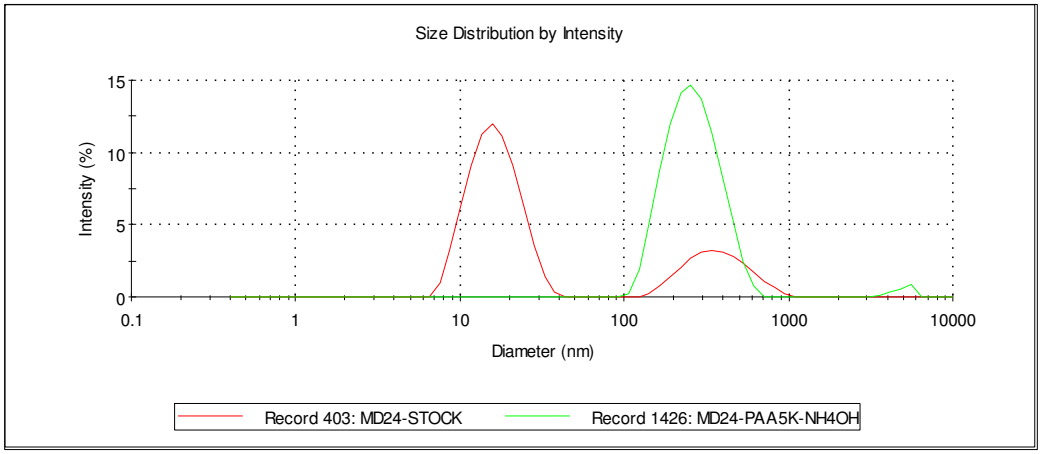

Figure 3.26: Micelle formation: Hydrodynamic size of stock solution MD24 (red) and polymer micelle (green).

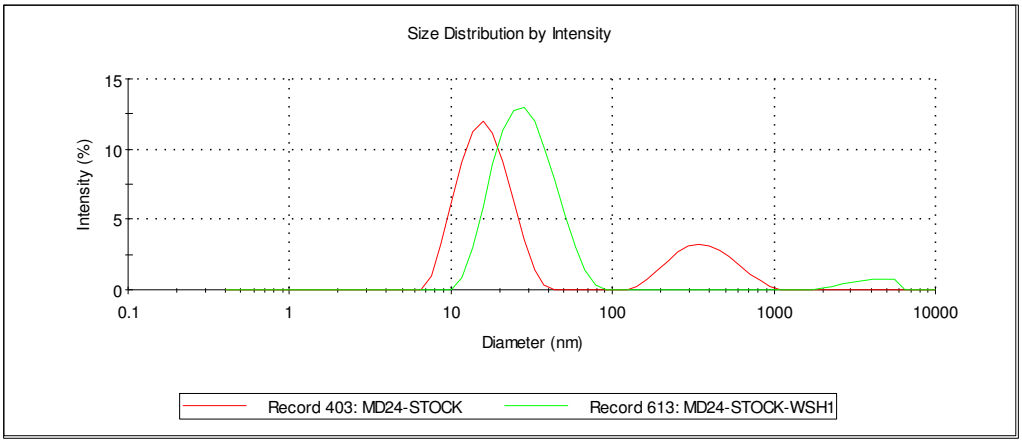

Figure 3.27: Removal of polymer micelle via ultrafiltration:
Stock solution of MD24 before (red) and after ultrafiltration (green).

Intensity size distribution peak width became narrower with low iron concentration and high reactive/Fe ratio (Table 3.5). This result may indicate effective surface coating per particle with the available excess polymer preventing aggregation.

Sample ID	Fe conc. (M)	Reactive/Fe (mol/mol)	Base ratio (mol/mol)	Mw of PAA (g/mol)	Peak width (nm)
MD22	**0.03**	**4**	**1**	**15000**	**6.51**
MD33	**0.03**	**4**	**1**	**5100**	**10.41**
MD28	**0.03**	**4**	**3**	**15000**	**12.19**
MD15	**0.16**	**2.15**	**2**	**5100**	**15.89**
MD24	**0.03**	**4**	**3**	**5100**	**17.38**
MD15R	**0.16**	**2.15**	**2**	**5100**	**23.01**
MD29	0.3	4	3	5100	31.85
MD25R	0.16	2.15	2	15000	35.38
MD23R	0.3	4	1	5100	40.23
MD17R	0.03	0.3	3	15000	64.51
MD20	0.03	0.3	1	5100	67.93
MD18RR	0.3	0.3	1	15000	70.14
MD21R	0.3	0.3	3	5100	72.42
MD26	0.03	0.3	3	5100	76
MD25	0.16	2.15	2	15000	81.85
MD32	0.03	0.3	1	15000	84.86
MD19	0.3	4	3	15000	96.63
MD27	0.3	0.3	3	15000	111.8
MD30	0.3	4	1	15000	155.6
MD31	0.3	0.3	1	5100	*

Table 3.5: Analysis of the size distribution of particles as a function of reaction variables. Narrow peak widths are highlighted with bold-face.

Polydispersity index of washed particles (PDI-wsh) were also evaluated to see the effect of reaction parameters. It was hard to see the responsible effects for PDI-wsh without statistical evaluations, so this will be detailed in Chapter 4.

Number intensity size distribution was also determined for all experiments in DLS measurements. There is a considerable difference between number intensity and intensity size distributions (Figure 3.28). Statistical evaluations were also done for hydrodynamic size based on number intensity size distribution), but particle sizes were so close to each other that it was not possible to deduct a correlation between the sizes and the variables. In this case, Design Expert 7.0 and Minitab 14 Release would be useless because no significant difference between reaction parameters can be found evaluating closer values. Also, standard deviations between center points and the difference between maximum and minimum value of hydrodynamic sizes were calculated for both intensity and number intensity size distributions of unwashed solutions. Table 3.6 shows that standard deviation and difference between maximum and minimum size for intensity size distribution is larger than number intensity size distribution. This wider range between sizes would provide more reasonable results in terms of statistics due to larger variety in values. Therefore, all hydrodynamic sizes used in statistical evaluations were based on the intensity size distribution peaks.

AFM studies showed us that the size that we observe generally correlate with the intensity based size distribution obtained by DLS. Therefore, we feel comfortable working with the intensity based numbers as a realistic approach.

Sample ID	Fe conc. (M)	Reactive/ Fe (mol/mol)	Base ratio (mol/mol)	Mw of PAA (g/mol)	Dh(I) unwsh (nm)	Dh(N) unwsh (nm)
MD33	0.03	4	1	5100	7	4
MD28	0.03	4	3	15000	28	16
MD29	0.3	4	3	5100	51	21
MD25	0.165	2.15	2	15000	164	10
MD31	0.3	0.3	1	5100	91	18
MD32	0.03	0.3	1	15000	142	16
MD27	0.3	0.3	3	15000	190	44
MD30	0.3	4	1	15000	220	16
MD15	0.165	2.15	2	5100	40	16
MD26	0.03	0.3	3	5100	122	28
MD22	0.03	4	1	15000	14	3
MD20	0.03	0.3	1	5100	91	38
MD25R	0.165	2.15	2	15000	79	40
MD18RR	0.3	0.3	1	15000	220	16
MD17R	0.03	0.3	3	15000	105	16
MD23R	0.3	4	1	5100	80	38
MD15R	0.165	2.15	2	5100	60	32
MD21R	0.3	0.3	3	5100	140	59
MD19RR	0.3	4	3	15000	150	21
MD24	0.03	4	3	5100	16	9
Standard deviation between center points					52.58	19.45
Difference between max. and min. value					213	56

Table 3.6: Standard deviation and difference between max. and min. values.

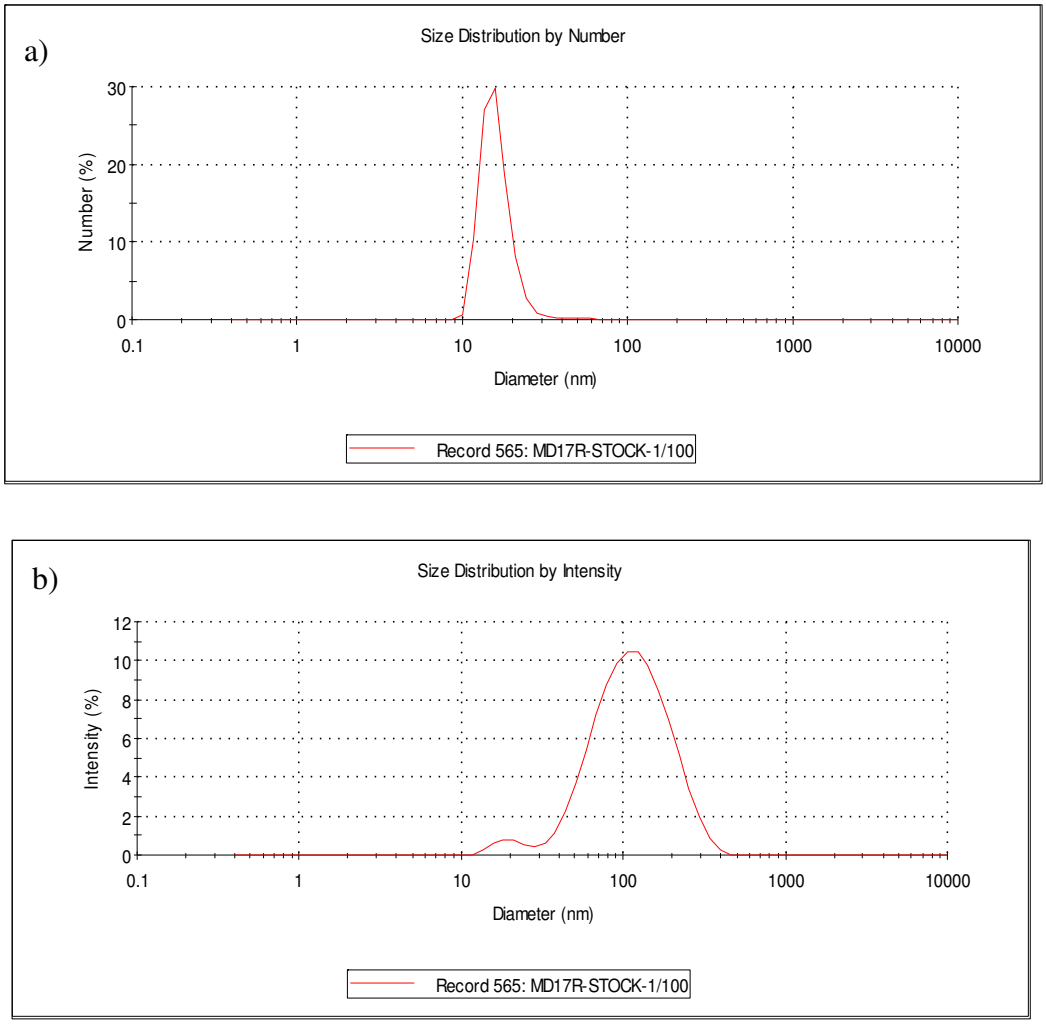

Figure 3.28: Difference between a) Number intensity size distribution (16 nm), b) Intensity size distribution (100 nm).

Chapter 4

STATISTICAL EVALUATIONS & DISCUSSION

4.1 Effective reaction parameters on particle size

Design Expert 7.0 and Minitab 14 Release statistical programs help to correlate the reaction factors with particle size. Best set of experiments were designed by the statistical programs for this purpose. Twenty systematic experiments with two center points per block were generated by the two-level full factorial design to evaluate also the interacting variables (Table 4.1).

In many general contexts, the "size" phenomenon is explained as a multiplicative (rather than additive) effect of its underlying factors. Taking the log will turn multiplicative effects into additive ones; therefore size data was analyzed after using log normal transformation.

Significant factors for particle size were found as iron concentration, reactive/iron mole ratio, molecular weight of PAA and interaction between iron concentration and reactive/iron mole ratio. Design Expert 7.0 provided "ANOVA Design" which showed the model as significant and displayed the significant factors based on p-values smaller than 0.05 (Table 4.2). Additionally, "Pareto Chart" showed the significant factors where four responsible reaction parameters passed beyond the p-value limit (Figure 4.1).

Sample ID	Fe conc. (M)	Reactive/Fe (mol/mol)	Base ratio (mol/mol)	Mw of PAA (g/mol)
MD15R	0.165	2.15	2	5100
MD25R	0.165	2.15	2	15000
MD15	0.165	2.15	2	5100
MD21R	0.3	0.3	3	5100
MD30	0.3	4	1	15000
MD29	0.3	4	3	5100
MD23R	0.3	4	1	5100
MD32	0.03	0.3	1	15000
MD26	0.03	0.3	3	5100
MD20	0.03	0.3	1	5100
MD17R	0.03	0.3	3	15000
MD25	0.165	2.15	2	15000
MD31	0.3	0.3	1	5100
MD27	0.3	0.3	3	15000
MD18RR	0.3	0.3	1	15000
MD19	0.3	4	3	15000
MD33	0.03	4	1	5100
MD22	0.03	4	1	15000
MD28	0.03	4	3	15000
MD24	0.03	4	3	5100

Table 4.1: Design space.

Response 1 Dh unw
Transform: Natural log Constant: 0
ANOVA for selected factorial model
Analysis of variance table [Partial sum of squares - Type III]

Source	Sum of Squares	df	Mean Square	F Value	p-value Prob > F	
Block	**8.148E-003**		**1**	**8.148E-003**		
Model	**15.56**	**4**	**3.89**	**23.26**	**< 0.0001**	**significant**
A-Fe	***4.59***	***1***	***4.59***	***27.46***	***0.0002***	
B-Acid/Fe	***5.57***	***1***	***5.57***	***33.34***	***< 0.0001***	
D-Mwt	***0.94***	***1***	***0.94***	***5.61***	***0.0355***	
AB	***3.60***	***1***	***3.60***	***21.51***	***0.0006***	
Curvature	**0.27**	**2**	**0.13**	**0.79**	**0.4747**	**not significant**
Residual	**2.01**	**12**	**0.17**			
Cor Total	**17.84**	**19**				

Table 4.2: ANOVA analysis for hydrodynamic size.

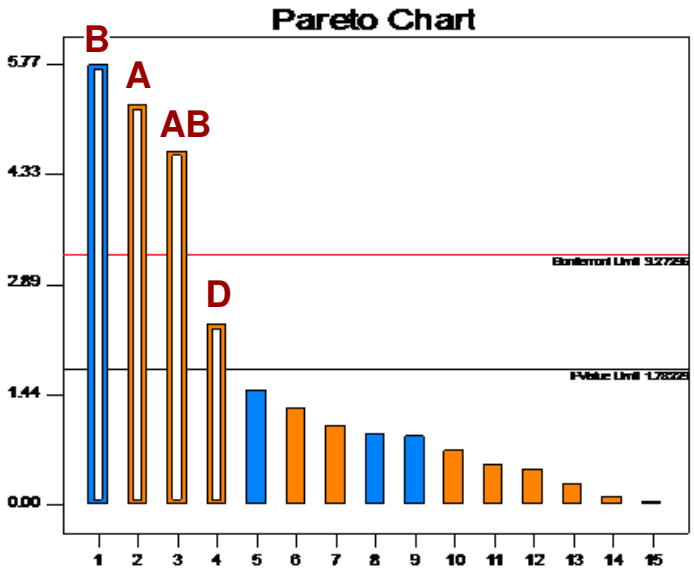

Figure 4.1: Pareto chart for hydrodynamic size after synthesis.

Minitab14 Release program was used to evaluate the four factors by using 'Main Effects Chart'. This data imply that nanoparticle size increases with increasing iron concentration and molecular weight of PAA and decreasing reactive/Fe mole ratio. This chart also indicates a negligible effect of base ratio (no dramatic change in slope) on particle size (Figure 4.2).

DLS data presented in previous chapter indicated that COOH/Fe ratio is influential on hydrodynamic size through some sort of interaction with other parameters, statistical evaluations here resolved these interactions. Two-way interaction plot analyses each factor in pairs. Crossing lines in Figure 4.3 indicates interacting factors. This data show that low iron concentration with high reactive/Fe ratio decreases particle size. Also it indicates that coating amount may change the particle size more dramatically in low Fe concentrations compared to high Fe concentrations. On a lesser extent, lower base ratio with higher molecular weight of polymer results an increase in particle size.

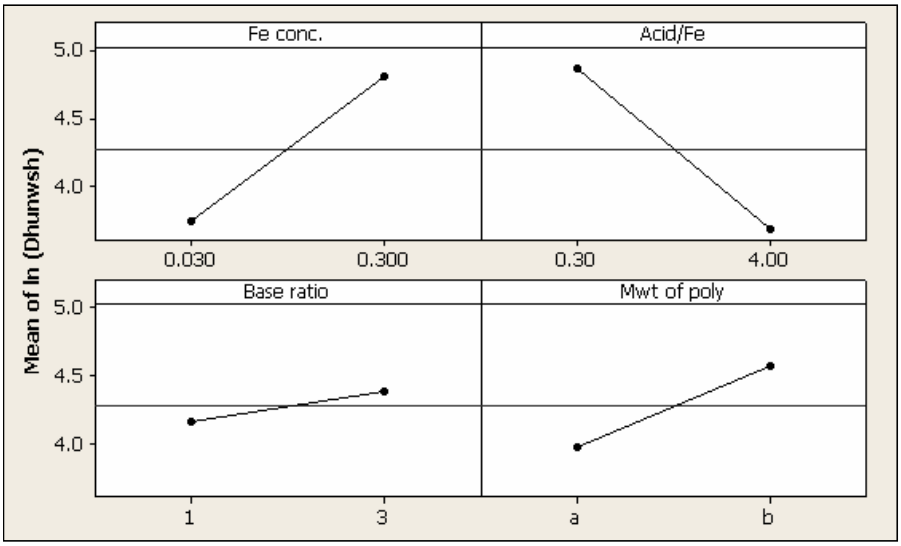

Figure 4.2: Main effects chart for hydrodynamic size after synthesis.

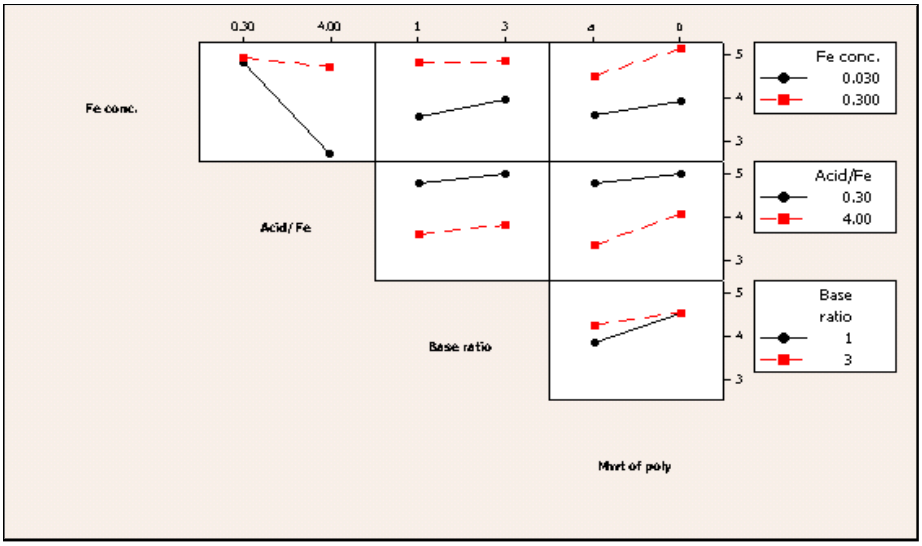

Figure 4.3: Interaction plot for hydrodynamic size after synthesis.

Hydrodynamic size was also evaluated after removal of excess coating material. Significant factors were found as Fe concentration and interaction of Fe concentration with reactive/Fe (Figure 4.4). The effect of each factor on particle size is shown in "Main Effects Chart" (Figure 4.5). This data imply that particle size increases with increasing Fe concentration and decreasing reactive/Fe ratio for washed particles. In addition, interaction plot showed that higher reactive/Fe ratio in concentrated solutions increases particle size while dilute solutions result in smaller size (Figure 4.6).

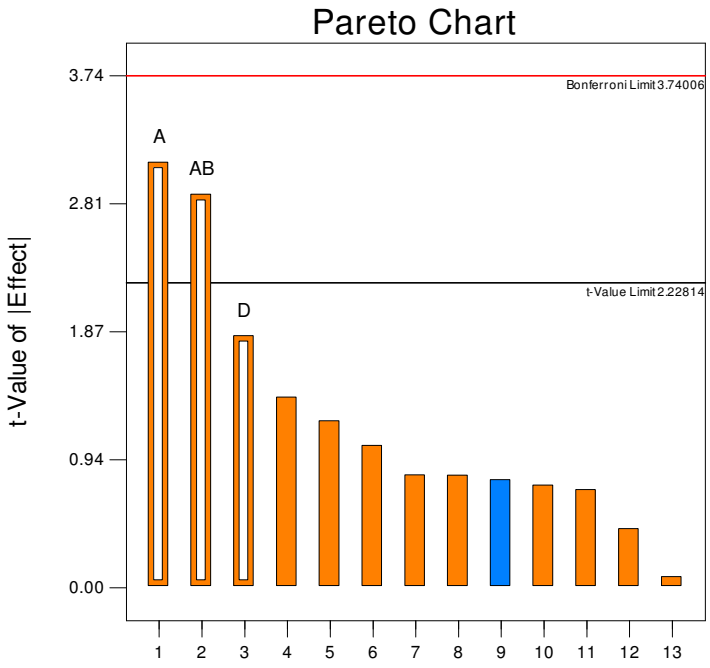

Figure 4.4: Pareto chart for hydrodynamic size after synthesis.

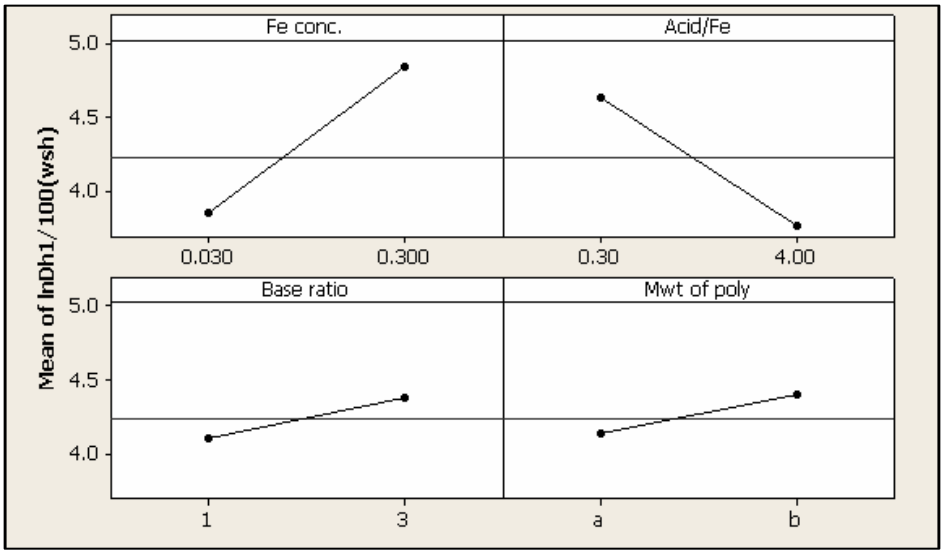

Figure 4.5: Main effects chart for hydrodynamic size after removal of excess polymer.

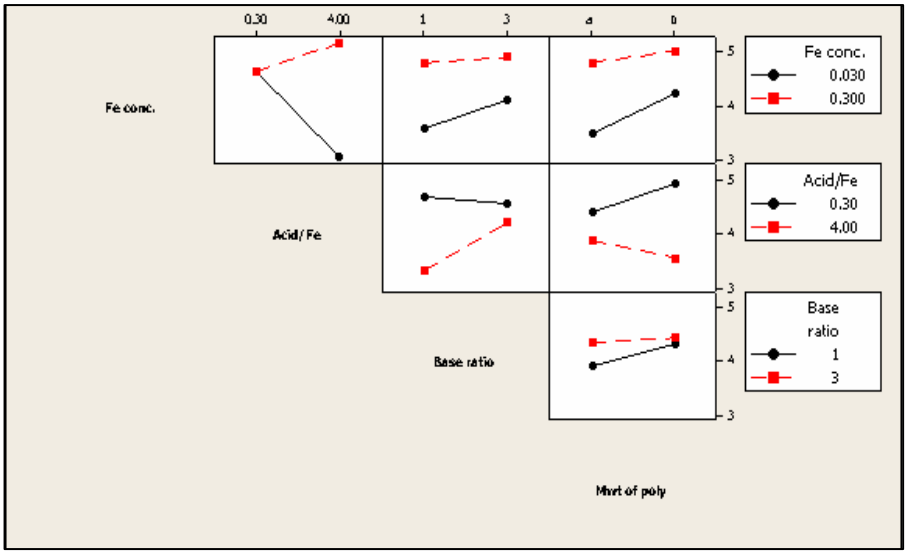

Figure 4.6: Interactions plot for hydrodynamic size after removal of excess polymer.

These observations may be explained by the following thinking: In reactions with high Fe concentrations, larger number of nucleation occurs and crystals grow faster than experiments with low iron concentration. Arresting particle growth through adsorption of polymer on the surface could possibly be more effective in dilute solutions where smaller number of crystals would form initially. This would provide each chain to adsorb on the particle through multiple points, more chains per particle and thicker coating which may also be the result of bridging between many polymer chains. Also, indication of size reduction with PAA of 5,100 g/mol would support this suggestion. As the size of the polymer chain increases bridging possibility increases (Figure 4.7).

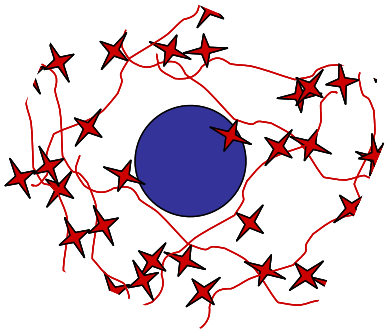

Figure 4.7: Bridging between polymer chains.

Furthermore, lower base ratio with higher molecular weight was found as an increasing factor for particle size in an interaction but from the slope of the lines it is a less dramatic influence (Figure 4.6). Although the lowest base amount was enough for both deprotanation of carboxylic acid groups and oxidation of iron salts, it was obvious that lower base ratio causes size distribution broadening as mentioned in previous chapter. The

possible explanation could be the adsorption of longer polymeric chains on multiple magnetic cores resulting an increase in particle size (Figure 4.8).

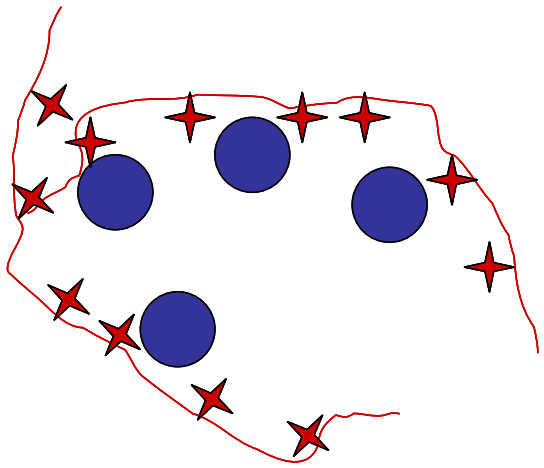

Figure 4.8: Adsorption of longer polymer chains on multiple cores.

Design Expert 7.0 fit a quantitative relation between these significant factors and the hydrodynamic size after synthesis (S). Equation (1) was created for PAA molecular weight 5,100 and (2) for molecular weight 15,000 g/mol where F was denoted for iron concentration and R was for reactive/Fe ratio.

$$Ln(S) = 4.73927 - 0.11358 \times F - 0.63233 \times R + 1.8986 \times F \times R \quad (1)$$

$$Ln(S) = 5.2235 - 0.11358 \times F - 0.63233 \times R + 1.89860 \times F \times R \quad (2)$$

Test experiments were also preformed to control the efficiency of equations (1) and (2). Equation (1) was used for all test experiments because only the constant value of equation (2) is different which makes 1.82 nm difference for the calculated particle size. Additionally, poly (methacrylic acid) sodium salt (PMAA) (Mw 6,500 g/mol) and

poly(acrylic acid) sodium salt (Mw 2,100 g/mol) were used in some of the experiments to check the applicability of the equation for different polymers with different molecular weights. Hydrodynamic sizes that are predicted by the equations and experimentally obtained are shown in Table 4.3. Experimental results were found within 10 nm deviation compared to predicted sizes which is quite good for hydrodynamic size measurements.

Fe conc. (M)	Reactive/ Fe (mol/mol)	Base ratio	Mw of PAA (g/mol)	Size (exp.)	Size (theo.)
0.18	2.8	2	5100	45	46.7
0.15	3	2	5100	25	37.1
0.1	3	2	5100	35	27.8
0.03	4	1.47	5100	11	10.7
0.03	4	3	5100	15	10.7
0.05	3	2	5100	30	20.9
0.03	0.3	3	2100	72	83.9
0.03	0.3	3	6500*	75	83.9

Table 4.3: Test experiments.

*Poly (methacrylic acid) sodium salt

Design Expert 7.0 also provided an equation for hydrodynamic size of particles after ultrafiltration with distilled water. However; missing values (*) in Table 3.1 lead to an incapable equation which could not predict particle size.

Furthermore, we tried to obtain a sufficient equation based on number intensity size distribution. This was also not satisfying due to the case of standard deviation between center points which was detailed in Chapter 3.

4.2 Statistical evaluations for stability

Stability of nanoparticles or in another word resistance to aggregation was checked by diluting samples up to 10,000 times with water. Statistical evaluation indicates that reactive/iron ratio is important for stability. Stable particles were denoted as 1 while unstable particle as 0, so to speak they were dead or alive. Therefore, the best way to analyze such data is simply the cube plots obtained from Minitab.

For lower molecular weight PAA, concentrated solutions with high reactive/iron ratio are stable and in case of higher molecular weigh PAA reactions higher iron concentrations with lower reactive/Fe ratio is desired for stability (Figure 4.9). This may indicate that longer chains might adsorb on different crystals at the same time, with much less contact of each chain on each crystal surface resulting in inferior stability. In this case, high iron concentration is favorable which may be due to fine crystal growth offering multiple adsorption sites. Here, it is important to note that hydrodynamic sizes reported for the size analysis were recorded from the 1/100 dilution as indicated before and they are all stable at this dilution.

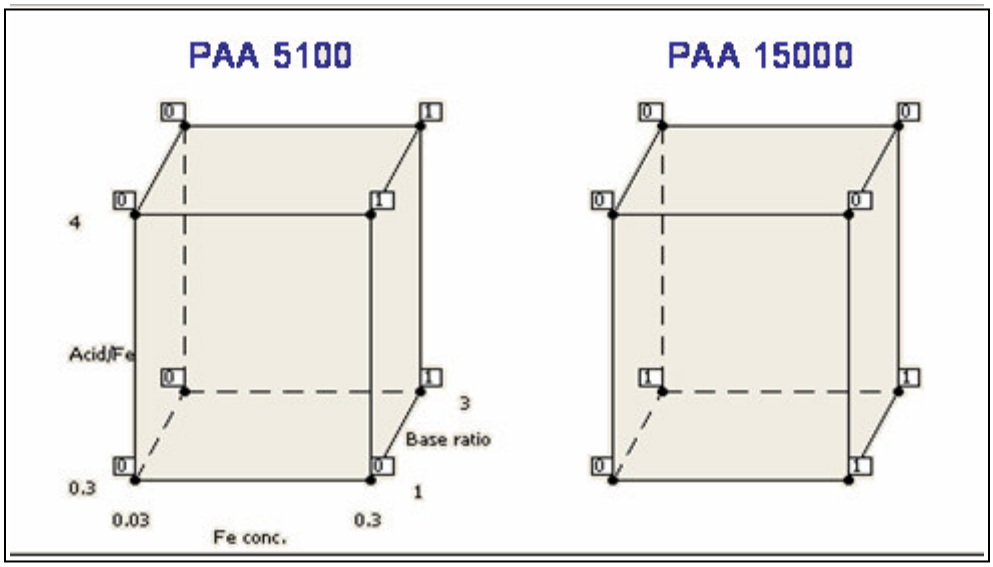

Figure 4.9: Cube plot for stability upon dilution of stock solution.

4.3 Statistical evaluations for magnetization

Particles must be magnetic otherwise useless for the suggested applications. Type of the magnetic core (magnetite or maghemite), interaction of the coating with the core, effective passification of the surface and prevention of oxidation as well as size and size distribution of the magnetic cores are important. Reactions were carried out at 85 ^{o}C to ensure magnetite formation [33]. Our preliminary studies showed that magnetization is highly correlated with base/reactive ratio and base ratio. The constraints for these parameters are as follows: Base/reactive $\geq$ 3 and base ratio $\geq$ 1. In these experiments, dried particles responding 0.3 T handheld magnet were recorded as magnetic and entered to the statistical programs as 1 for magnetic and 0 for non-magnetic. Statistical data showed that high reactive/Fe ratio along with low Fe concentration produces non-magnetic materials (Figure 4.10). In previous chapter, these reaction parameters were found responsible from

less intense peaks in X-Ray diffraction peaks. The same reason is valid for non-magnetic particles, which is too much coating material prevents crystal growth and may be also nucleation so that magnetization could not be observed in those particles.

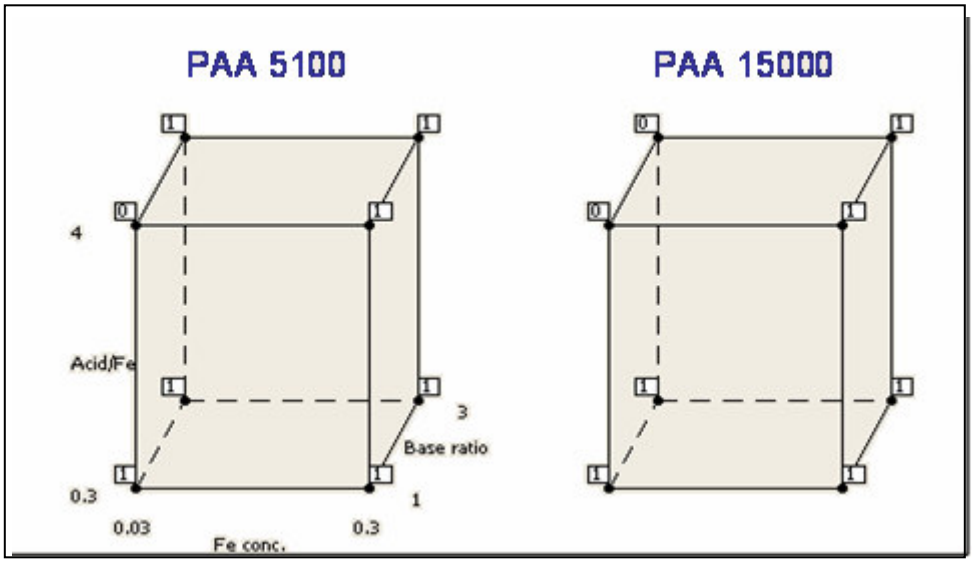

Figure 4.10: Cube plot for magnetization of stock solution.

4.4 Miscallenous

In previous chapter, bimodality and intensity size distribution peak width were correlated with reaction parameters. Polydispersity index of washed particles (PDI-wsh) was not observed clearly so that statistical evaluations were performed. Interaction between molecular weight of poly(acrylic acid) sodium salt and reactive/Fe ratio was found effective. PDI-wsh increases with increasing reactive/Fe ratio for high PAA molecular weight. However, with the low PAA molecular weight, PDI-wsh decreases as the reactive/Fe ratio increases (Figure 4.11). This can be also viewed as many small chains are better than few long chains in terms of PDI, and actually true for the size as we have seen before. This interesting result indicates that longer chains cause broader size distribution

through bridging between particles and higher degree of chain entanglement. Yet, if we have too low concentration of the COOH units, effective coating of particles would not be achieved causing particle aggregation, uncontrolled growth and inferior stability against aggregation.

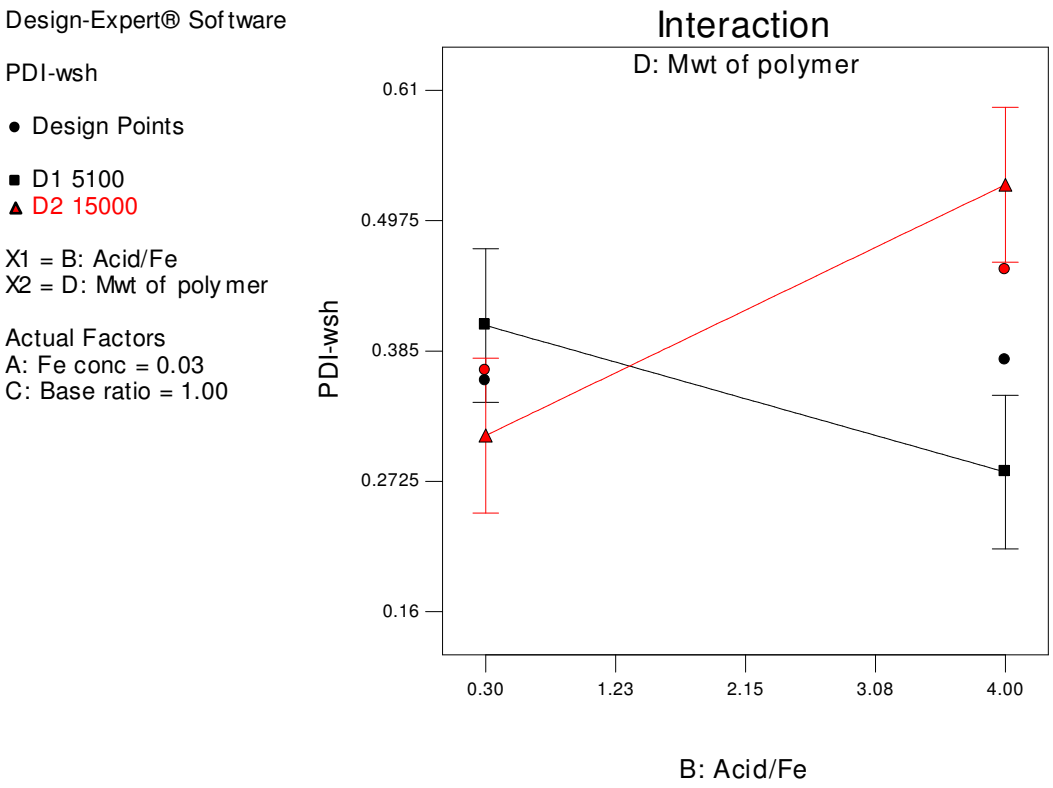

Figure 4.11: Interaction plot of polymer Mwt and Acid/Fe ratio for PDI of washed nanoparticles.

Chapter 5

IN VITRO STUDIES

Five different doses of washed and filtered MD24 (30 nm), MD17R (80nm) and MD32 (110 nm) were used for contrast enhancement studies. Endorem® (140nm), commercial contrast agent, was used as a reference for comparison with our samples. Signal intensities are shown in Table 5.1 and plotted versus five doses (Figure 5.1).

	Signal Intensity			
Fe (mM)	**Endorem®**	**MD17**	**MD24**	**MD32**
0.4	**399.5**	**575.3**	**343**	**220.7**
0.2	**347.1**	**487**	**235.5**	**156.1**
0.1	**206**	**360.9**	**160.5**	**142.9**
0.05	**217.6**	**131.7**	**137.3**	**136.4**
0.025	**189.1**	**144.3**	**110.5**	**128.3**
0	**135.6**	**82**	**70.1**	**111**
% increase	**195**	**602**	**389**	**99**

Table 5.1: Signal intensity of samples.

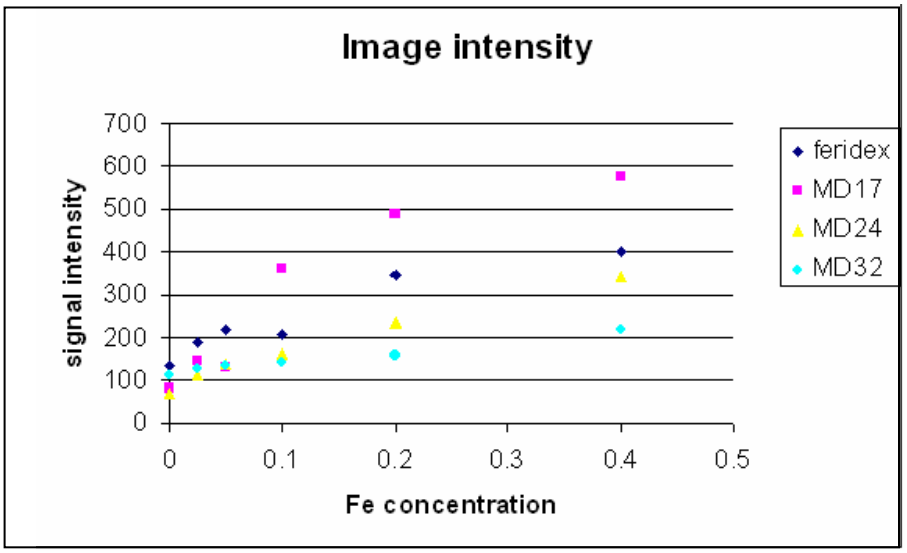

Figure 5.1: Signal intensity distribution of particles for five different doses of iron.

Signal intensity evaluations and MRI image (Figure 5.2) showed that MD24 and MD17R seem to be a better T1 agent compared to Endorem®.

In addition, preliminary cytotoxicity tests of these samples were preformed. HeLa and MCF-7 cancer cells were incubated with our samples and cell viabilities were measured by MTT assay. Preliminary results indicate non-toxic behavior of the particles to the cells.

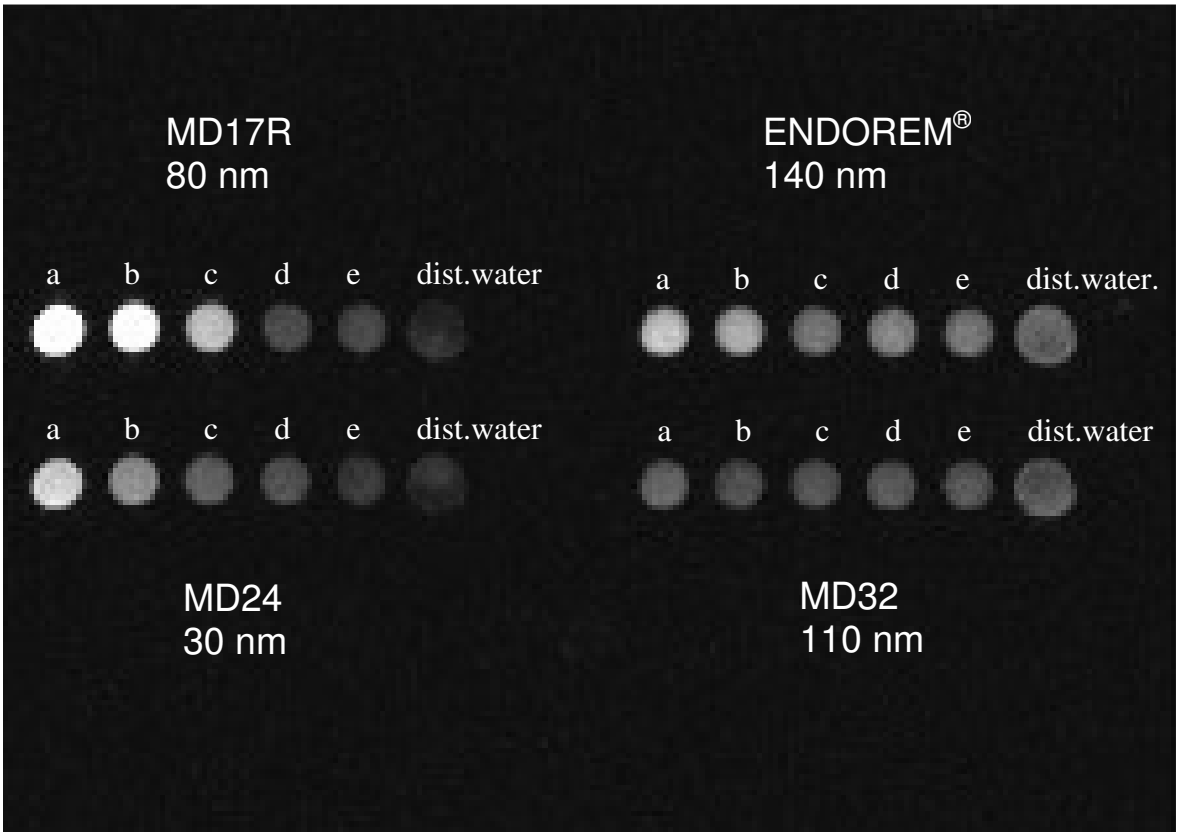

Figure 5.2: MRI image of samples compared to Endorem®

[Fe]: a) 0.4mM, b) 0.2 mM, c) 0.1 mM, d) 0.05 mM, e) 0.025 mM.

Chapter 6

CONCLUSIONS

In this research, poly (acrylic acid) coated iron oxide nanoparticles were synthesized in aqueous solutions with varying experimental parameters. These parameters were selected as iron concentration, reactive/Fe ratio, base ratio and molecular weight of polymer. Design Expert 7.0 and Minitab 14 Release statistical programs were used to evaluate the effective reaction parameters on hydrodynamic size, stability and magnetization.

Iron concentration, reactive/Fe molar ratio, molecular weight of PAA and Fe concentration*Reactive/Fe interaction were found significant in affecting the *hydrodynamic size* of the particles. Hydrodynamic size increases with increasing Fe concentration and molecular weight of PAA, and decreasing reactive/Fe ratio. In addition, second order interactions between reaction parameters also have a considerable effect on hydrodynamic size. It was found that low iron concentration with high Reactive/Fe ratio decreases particle size. This can be due to availability of more coating material per crystal resulting in more efficient surface passifisation and better electrostatic/ steric stabilization. Also, lower base ratio with higher molecular weight of polymer seems to increase particle size. This can be evaluated as the adsorption of longer polymer chains on multiple cores resulting an increase in particle size.

Design Expert 7.0 provided a quantitative relation between particle size and significant factors. Test runs showed quite a good agreement between experimental and predicted

values. Target hydrodynamic sizes were achieved within 10 nm deviation. Predictions can be extended to other experiments which were performed with poly (methacrylic acid) and PAA (Mw 2000 g/mol) with same accuracy.

Effective factor for *dilution stability* was found as Reactive/Fe mole ratio. According to the statistical evaluations, dilution stability requires high concentration of iron with many small chains (low molecular weight with high reactive/Fe ratio) rather than few long chains of PAA (high Mw PAA with low reactive/Fe ratio). Long polymer chains can adsorb on a number of crystals simultaneously resulting in larger Dh but also this would lead into less interaction between the coating and crystal surface resulting easier detachment of coating material. On the other hand, high reactive/Fe ratio and Fe concentration increase solution viscosity and cause precipitation within few days. In order to overcome this problem, stock solution can be diluted after synthesis but this method will not work for obtaining target hydrodynamic sizes.

Factors increasing the hydrodynamic size also increased the size distribution which is again following the basic idea of bridging polymers with high polymer molecular weight and effective coating of each particle with increasing coating amount.

In case of magnetization, high reactive/Fe ratio along with low Fe concentration produces non-magnetic materials. This may indicate the insufficient crystal growth in the presence of too much coating material.

In summary, the influence of responsible factors on hydrodynamic size (1/100 dilution of stock solution), stability (after synthesis and removal of excess polymer) and magnetization is shown in Table 6.1.

Factors	D_h	Stability unwsh	Stability wsh	Magn.
Fe conc. ↑	↑	↑	↑	↑
Reactive/Fe ↑	↓	↓	↓	↓
Base ratio ↑	↔	↔	↔	↔
Mw of PAA ↑	↑	↓	↔	↓

Table 6.1: The way that factors influence responses.

Poly (acrylic acid) sodium salt was used as a polymeric coating around iron oxide core. Carboxylic acid groups provided surface functionality to the particles such as pH sensitivity. The pH and ionic strength of the solution play an important role in stabilizing magnetic particles with electrostatic repulsion. Under acidic conditions, carboxylic acid groups have less ionic strength, so interaction between particles changes to attraction rather than repulsion resulting particle aggregation. In addition, PAA sodium salt provided steric stabilization due to the difficulty of interpenetration between polymer chains.

X-Ray diffraction peaks showed that PAA-coated iron oxide nanoparticles have the composition of both Fe_3O_4 and gamma-Fe_2O_3. In some of the experiments, diffraction peaks were not intense due to the insufficient crystal growth in the presence of excess coating material. In addition, core size was calculated with Scherer's equation and size sizes were found between 5 to 40 nanometers for different preparations.

Transmission electron microscopy has shown the morphology of the composite particles. TEM micrographs showed a grainy morphology rather than spherical which indicates the polymeric shell around iron oxide cores.

Atomic force microscope (AFM) images helped to observe particle size and size distribution. Hydrodynamic sizes measured by DLS (based on intensity) were also confirmed with AFM images.

The hysteresis curves of some samples were also studied by Vibrating Sample Magnetometer (VSM). PAA-coated iron oxide nanoparticles demonstrate a lower magnetic saturation (10 emu/g sample) as compared to pure Fe_3O_4 nanoparticles due to the formation of Fe_2O_3 crystals during synthesis. Furthermore, the remanence and coercivity were zero, and there was no hysteresis loop. These results indicate that iron oxide nanoparticles synthesized in the presence of poly (acrylic acid) sodium salt were superparamagnetic.

In vitro studies were done with three different sizes (30, 80 and 110 nm) of iron oxide nanoparticles. Preliminary MRI studies showed that our sample (particle size 80 nm) could be a better T1 contrast agent than the commercial product, Endorem®. Also, these three samples did not show non-toxic behavior with HeLa and MCF-7 cancer cells.

All in all, this research provided the opportunity to obtain surface functional, stable and aqueous superparamagnetic iron oxide nanoparticles. In situ coating method provided us to obtain water-based stable ferrofluids of small and ultrasmall sizes without size separation process. Results obtained in this project provide a new and simple method to control particle size and stability at the synthesis step and an understanding of the limitation in adjusting reaction factors to have all the desired properties.

Appendix A

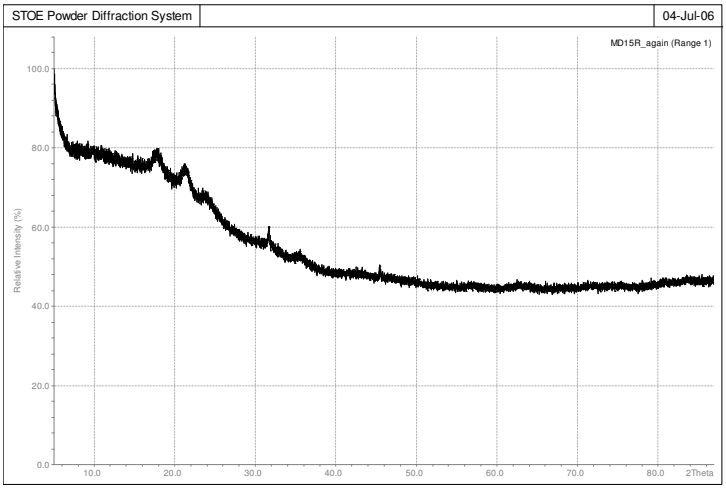

Figure A-1: XRD diagram of MD15R.

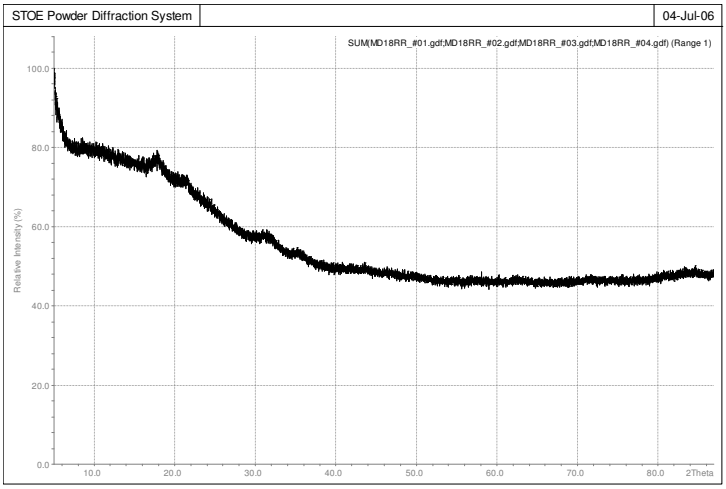

Figure A-2: XRD diagram of MD18RR.

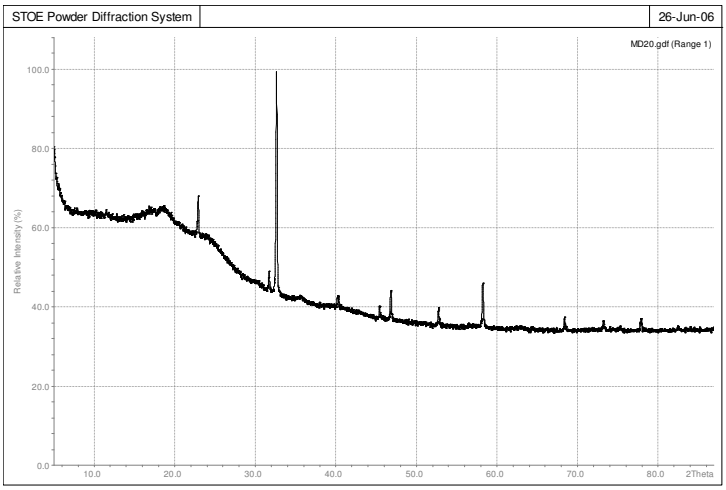

Figure A-3: XRD diagram of MD20.

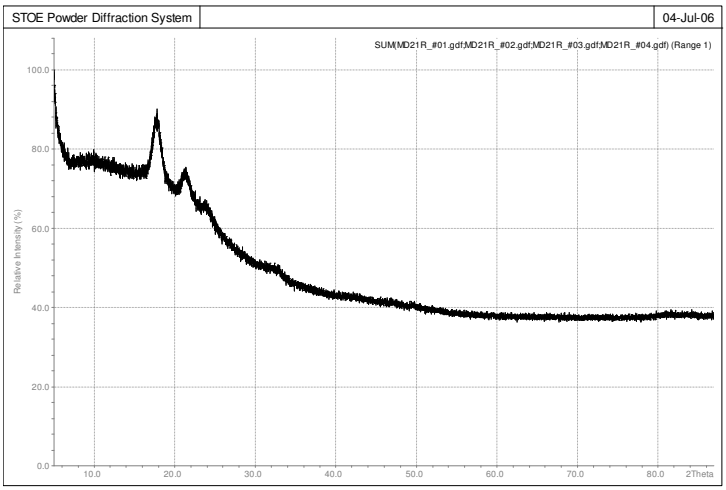

Figure A-4: XRD diagram of MD21R.

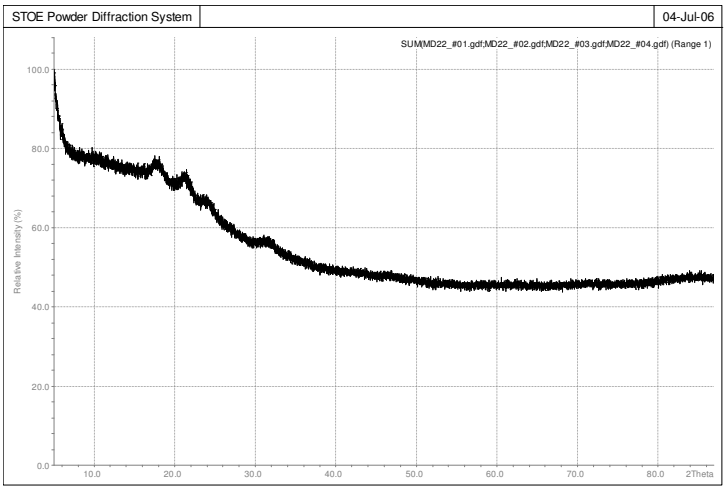

Figure A-5: XRD diagram of MD22.

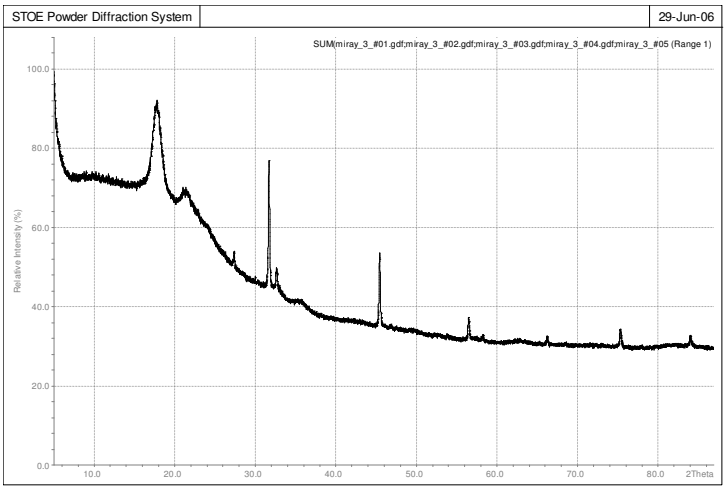

Figure A-6: XRD diagram of MD23R.

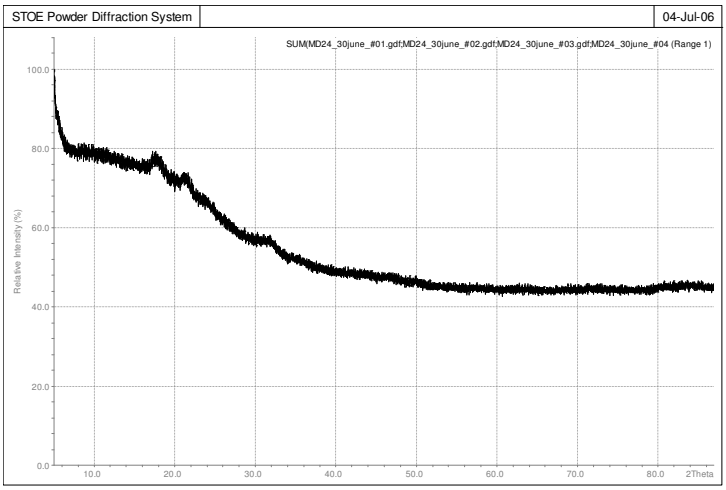

Figure A-7: XRD diagram of MD24.

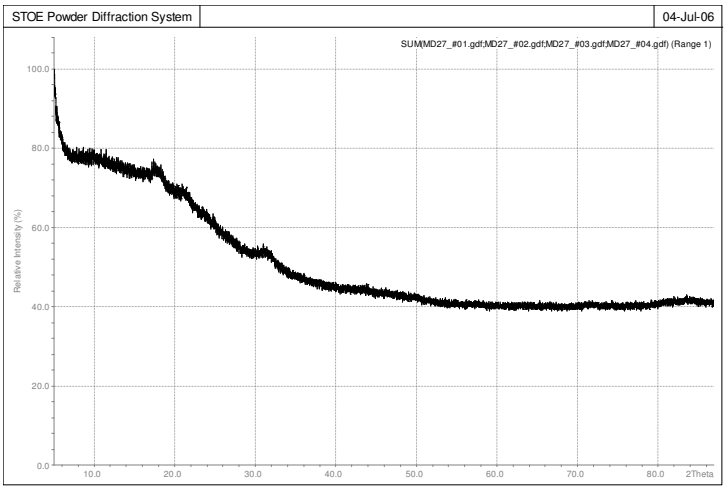

Figure A-8: XRD diagram of MD27.

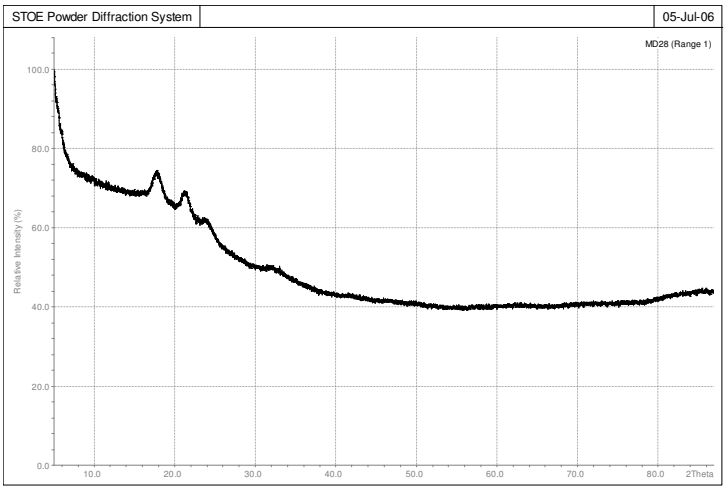

Figure A-9: XRD diagram of MD28.

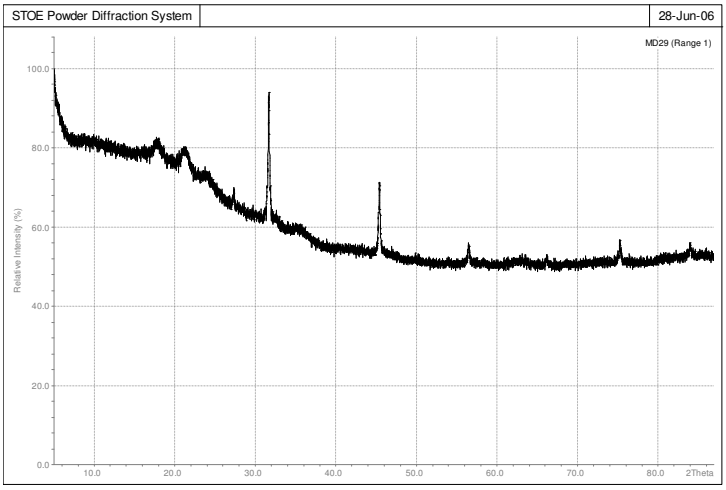

Figure A-10: XRD diagram of MD29.

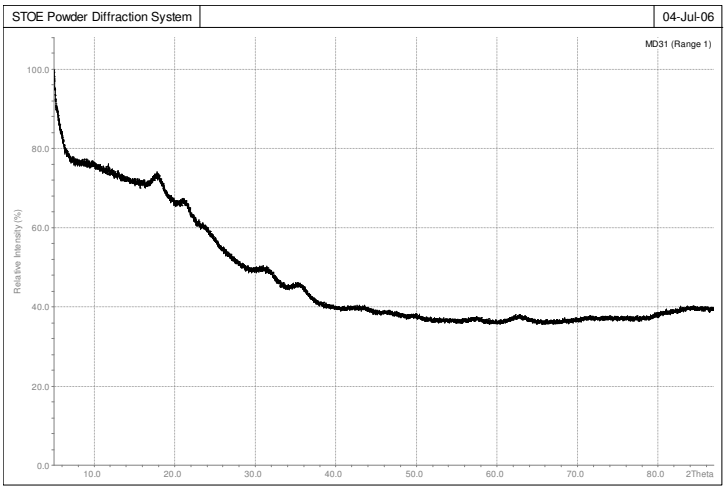

Figure A-11: XRD diagram of MD31.

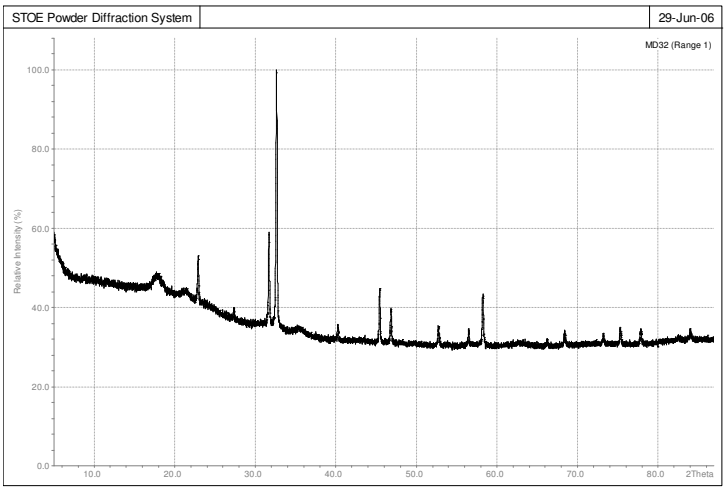

Figure A-12: XRD diagram of MD32.

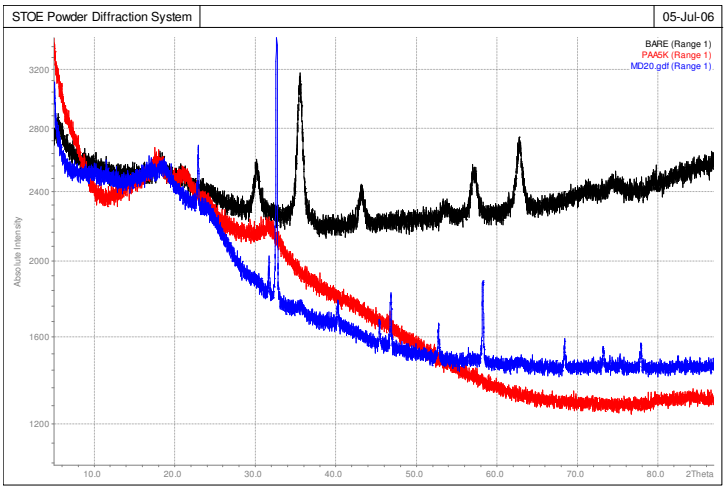

Figure A-13: XRD diagram of bare nanoparticles (black), pure poly(acrylic acid) sodium salt (red), PAA-coated iron oxide nanoparticles (MD20).

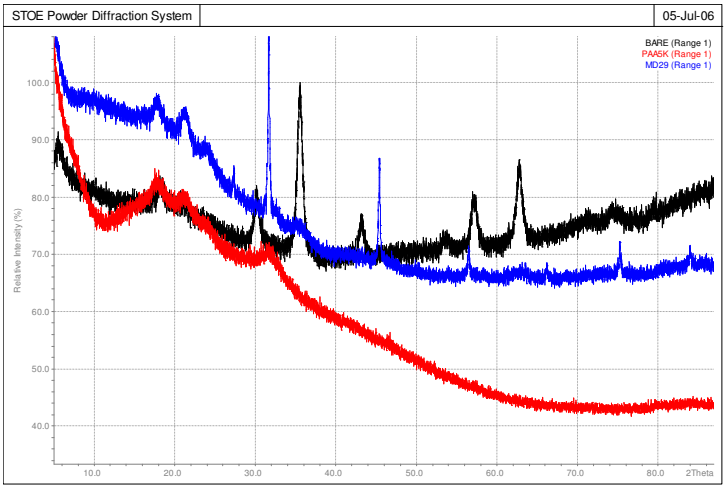

Figure A-13: XRD diagram of bare nanoparticles (black), pure poly(acrylic acid) sodium salt (red), PAA-coated iron oxide nanoparticles (MD29).

BIBLIOGRAPHY

[1] Q.A. Pankhurst, J. Connolly, S.K. Jones and J. Dobson, Applications of magnetic nanoparticles in biomedicine, J. Phys. D: Appl. Phys. 36 (2003) R167–R181.

[2] C.C. Berry1, A.S.G. Curtis, Functionalisation of magnetic nanoparticles for applications in biomedicine, J. Phys. D: Appl. Phys. 36 (2003) R198–R206.

[3] A. Ito, M. Shinkai, H. Honda, T. Kobayashi, Medical application of functionalized magnetic nanoparticles, Journal of Bioscience and Bioengineering 100 (2005) 1–11.

[4] O.V. Salata, Applications of nanoparticles in biology and medicine, Journal of Nanobiotechnology 2:3 (2004).

[5] T. Neubergera, B. Schopf, H. Hofmann, M. Hofmann, B. von Rechenberga, Superparamagnetic nanoparticles for biomedical applications: Possibilities and limitations of a new drug delivery system, Journal of Magnetism and Magnetic Materials 293 (2005) 483–496.

[6] J. Chatterjee, Y. Haik, C.J. Chen, Size dependent magnetic properties of iron oxide nanoparticles, Journal of Magnetism and Magnetic Materials 257 (2003) 113–118.

[7] K.Y. Wina, S.S. Feng, Effects of particle size and surface coating on cellular uptake of polymeric nanoparticles for oral delivery of anticancer drugs, Biomaterials 26 (2005) 2713–2722.

[8] R.M. Cornell, U. Schwertmann, The Iron Oxides, VCH Publishers (1996) 117.

[9] W. Jianga, H.C. Yang, S.Y. Yang, H.E. Horng, J.C. Hung, Y.C. Chen, C.Y.Hong, Preparation and properties of superparamagnetic nanoparticles with narrow size distribution and biocompatible, Journal of Magnetism and Magnetic Materials 283 (2004) 210–214.

[10] C. Alexiou, W. Arnold, P. Hulin, R.J. Klein, H. Renz, F.G. Parak, C. Bergemann, A.S. Lubbe, Magnetic mitoxantrone nanoparticle detection by histology, X-ray and MRI after magnetic tumor targeting, Journal of Magnetism and Magnetic Materials 225 (2001) 187-193.

[11] B. Schopf, T. Neuberger, K. Schulze, A. Petri, M. Chastellain, M. Hofmann, H. Hofmann, B. von Rechenberg, Methodology description for detection of cellular uptake of PVA coated superparamagnetic iron oxide nanoparticles (SPION) in synovial cells of sheep, Journal of Magnetism and Magnetic Materials 293 (2005) 411–418.

[12] B.S. Kim, J.M. Qiu, J.P. Wang, T.A. Taton, Magnetomicelles: Composite nanostructures from magnetic nanoparticles and cross-Linked amphiphilic block copolymers, Nanoletters 5 (2005) 1987-1991.

[13] Y. Lu, J. McLellan, Y. Xia, Synthesis and crystallization of hybrid spherical colloids composed of polystyrene cores and silica shells, Langmuir 20 (2004) 3464-3470.

[14] A.K. Gupta, S. Wells, Surface-modified superparamagnetic nanoparticles for drug delivery: Preparation, characterization, and cytotoxicity studies, IEEE Transactions on Nanobioscience 3 (2004).

[15] H. Choi, S.R Choi, R. Zhou, H.F. Kung, I.W. Chen, Iron oxide nanoparticles as magnetic resonance contrast agent for tumor imaging via folate receptor-targeted delivery, Academic Radiology 11 (2004) 996-1004.

[16] R. Weissleder, Scaling down imaging: Molecular mapping of cancer in mice, Nature Reviews 2 (2002) 1-8.

[17] C. Dromain, T. de Baere, E. Baudin, J. Galline, M. Ducreux, V. Boige, P. Duvillard, A. Laplanche, H. Caillet, P. Lasser, M. Schlumberger, R. Sigal, MR imaging of hepatic metastases caused by neuroendocrine tumors: Comparing four techniques, American Journal of Roentology 180 (2003) 121-128.

[18] A.E. Merbach, E. Toth, The chemistry of contrast agents in magnetic resonance imaging, John&Wiley Pub. 2001.

[19] C. Alexiou, R. Jurgons, R.J. Schmid, C. Bergemann, J. Henke, W. Erhardt, E. Huenges, F. Parak, Magnetic drug targeting: Biodistribution of the magnetic carrier and the chemotherapeutic agent mitoxantrone after locoregional cancer treatment, Journal of Drug Targeting 11 (2003) 139–149.

[20] A. Jordan, R. Scholz, K. Maier-Hauff, F.K. van Landeghem, N. Waldoefner, U. Teichgraeber, J. Pinkernelle, H. Bruhn, F. Neumann, B. Thiesen, A. von Deimling, R. Felix, The effect of thermotherapy using magnetic nanoparticles on rat malignant glioma, Journal of Neurooncology 78 (2006) 7-14.

[21] K. Raj, B. Moskowitz, R. Casciari, Advances in ferrofluid technology, J. Magn. Magn. Mater. 149 (1995) 174–180.

[22] A.K. Gupta, M. Gupta, Synthesis and surface engineering of iron oxide nanoparticles for biomedical applications, Biomaterials 26 (2005) 3995-4021.

[23] T. Hyeon, S.S. Lee, J. Park, Y. Chung, H. Bin Na, Synthesis of highly crystalline and monodisperse maghemite nanocrystallites without a size-selection process, J. Am. Chem. Soc. 123 (2000) 12798-12801.

[24] A.K. Gupta, A.S.G. Curtis, Lactoferrin and cerulosplasmin derivatized superparamagnetic iron oxide nanoparticles for targeting cell surface receptors, Biomaterials 25 (2004) 3029-3040.

[25] D.K. Kim, Y. Zhang, W. Voit, K.V. Rao, M. Muhammed, Synthesis and characterization of surfactant-coated superparamagnetic monodispersed iron oxide nanoparticles, Journal of Magnetism and Magnetic Materials 225 (2001) 30-36.

[26] C.L. Lin, C.F. Lee, W.Y. Chiu, Preparation and properties of poly(acrylic acid) oligomer stabilized superparamagnetic ferrofluid, Journal of Colloid and Interface Science 291 (2005) 411–420.

[27] D.H. Chen, S.H. Huang, Fast separation of bromelain by polyacrylic acid-bound iron oxide magnetic nanoparticles,

[28] D.H. Chen, Y.Y. Chen, Synthesis of strontium ferrite nanoparticles in the presence of poly (acrylic) acid, Materials Research Bulletin 37 (2002) 801-810.

[29] A.J. Rondinone, A.C.S. Samia, Z.J. Zhang, A chemometric approach for predicting the size of magnetic spinel ferrite nanoparticles from the synthesis conditions, J. Phys. Chem. B 2000, 104, 7919-7922.

[30] R.D. Waldron, Phys. Rev. 99 (1995) 1727–1735.

[31] N. Shukla, C. Liu, P.M. Jones, D. Weller, FTIR study of surfactant bonding to FePt nanoparticles, J. Magn. Magn. Mater. 266 (2003) 178–184.

[32] Q. Liu, Z. Xu, Self-assembled monolayer coatings on nanosized magnetic particles using 16-mercaptohexadecanoic acid, Langmuir 11 (1995) 4617-4622.

[33] L. Shen, P.E. Laibinis, T. A. Hatton, Bilayer surfactant stabilized magnetic fluids: Synthesis and interactions at interfaces, Langmuir 15 (1999) 447-453.

VITA

Miray Demirer was born in Bursa, Turkey in 1981. She completed the high school in Istanbul Ataturk Fen Lisesi in 1999. She received her B.S. degree from Department of Chemistry, Istanbul Technical University in 2003. In 2004, she started her M.S. degree in Material Science& Engineering department at Koc University.